

Title:

Binding of the integrated stress response inhibitor ISRIB reveals a regulatory site in the nucleotide exchange factor, eIF2B

One Sentence Summary:

Cryo-electron microscopy and chemogenetic selection define an ISRIB binding pocket in the core of the eIF2B decamer.

Authors:

Alisa F. Zyryanova^{1,*}, Félix Weis^{1-4,†}, Alexandre Faille^{1-3,†}, Akeel Abo Alard⁵, Ana Crespillo-Casado¹, Yusuke Sekine¹, Heather P. Harding¹, Felicity Allen⁶, Leopold Parts⁶, Christophe Fromont⁵, Peter M. Fischer⁵, Alan J. Warren^{1-4,*} and David Ron^{1,*}

Affiliations:

¹Cambridge Institute for Medical Research, University of Cambridge, Cambridge CB2 0XY, United Kingdom

²Department of Haematology, University of Cambridge, Cambridge, UK

³Wellcome Trust–Medical Research Council Stem Cell Institute, University of Cambridge, Cambridge, UK.

⁴MRC Laboratory of Molecular Biology Francis Crick Avenue Cambridge UK CB2 0QH

⁵Division of Biomolecular Science & Medicinal Chemistry, School of Pharmacy, University of Nottingham, Nottingham UK NG7 2RD

⁶Wellcome Trust Sanger Institute, Wellcome Genome Campus, Hinxton, Cambridgeshire, UK CB10 1SA

*Corresponding authors. Email: az310@cam.ac.uk (AZ), ajw1000@cam.ac.uk (AJW), dr360@medschl.cam.ac.uk (DR)

†These authors contributed equally to this work.

Abstract:

The Integrated Stress Response (ISR) is a conserved translational and transcriptional program affecting metabolism, memory and immunity. The ISR is mediated by stress-induced phosphorylation of translation initiation factor 2 α (eIF2 α) that attenuates the guanine nucleotide exchange factor eIF2B. A chemical inhibitor of the ISR, ISRIB, reverses the attenuation of eIF2B by phosphorylated eIF2 α , protecting mice from neurodegeneration and traumatic brain injury. We describe a 4.1 Å resolution cryo-electron microscopy structure of human eIF2B with an ISRIB molecule bound at the interface between the β and δ regulatory subunits. Mutagenesis of residues lining this pocket altered the hierarchical cellular response to ISRIB analogs in vivo and ISRIB-binding in vitro. Our findings point to a site in eIF2B that can be exploited by ISRIB to regulate translation.

Main text:

The Integrated Stress Response (ISR) has homeostatic functions that increase fitness. However, in some pathological circumstances benefit arises from attenuated signaling in the ISR (1). A search for ISR inhibitors led to the discovery of ISRIB (2), a small molecule efficacious in mouse models of neurodegeneration (3) and traumatic brain injury (4).

ISRIB action converges on eIF2B, a protein complex with guanine nucleotide exchange (GEF) activity towards eIF2 (5) that is inhibited by phosphorylated eIF2 (6, 7). Addition of ISRIB accelerates eIF2B GEF activity in vitro and targeting eIF2B's δ regulatory subunit can impart ISRIB resistance (8, 9). However, known ISRIB-resistant mutations in eIF2B cluster at a distance from both the regulatory site engaged by eIF2(α P) and the catalytic site engaged by eIF2 γ (10). Thus, whilst the bulk of the evidence suggests that ISRIB binds eIF2B to regulate its activity, indirect modes of action are not excluded.

ISRIB stabilized the eIF2B complex from HeLa cells (Fig. S1), as expected (9). Thus, we added a fluorescently labeled derivative of ISRIB (AAA2-101) (Fig. S2A) to purified eIF2B and observed increased fluorescence polarization (FP) (Fig. 1A-left panel). Unlabeled ISRIB competed for eIF2B in the FP assay with an EC₅₀ in the nanomolar range (Fig. 1A-right panel). As observed for ISRIB action in cells, less active analogs competed less successfully (Fig. S2B & S2C).

We purified endogenous eIF2B from HeLa cell lysates in the presence of ISRIB and determined the structure of the complex by single particle cryo-electron microscopy at an overall resolution of 4.1 Å (Fig. 1B, S1A, S3 and table S6). Within the β and δ regulatory core, protein side chains were clearly resolved, resulting in a near complete

atomic model of this region (Fig. 1C, S4A & S4B). The resolution of the γ and ϵ human catalytic subcomplex was lower compared with the regulatory core (Fig S4A) and the catalytically important C-terminal HEAT domain of the ϵ subunit remained unresolved in the cryo-EM map.

Owing to a lack of sufficient high-quality cryo-EM images of an apo-eIF2B complex, we were unable to calculate a difference map of eIF2B with and without ISRIB. However, a nearly continuous density with a shape and size of a single ISRIB molecule was conspicuously present at the interface of the β and δ regulatory subunits (Fig. 1B, “central view” & S4C). The ISRIB binding pocket was located at the plane of symmetry between the β and δ subunits. In the central part of the pocket, the side chain of β H188 was positioned in the vicinity of the essential carbonyl moiety of ISRIB (11) and β N162 was poised to stabilize the diaminocyclohexane moiety of ISRIB through hydrogen bonding interactions (Fig. 1D). More distally the side chains of δ L179, δ F452, δ L485, δ L487, β V164, β I190, β T215, and β M217 formed the hydrophobic end of the symmetrical pocket that accommodated the aryl groups of ISRIB, with β I190 and δ L179 located within Van der Waals interaction distance to the aryl group (Fig. S4D). A hamster *Eif2b4*^{L180F} mutation (δ L179 in the human) disrupts ISRIB action in cells (8), which is consistent with a potential loss of these interactions as well as a clash between the bulkier side chain of phenylalanine and the bound ISRIB molecule (Fig. 1D).

Overall the human structure is highly similar to the published *S. pombe* eIF2B structure (10) (r.m.s.d. of 2.57 Å over 3049 alpha carbons, Fig. S4E). However, there is no density

in the corresponding region in the *S. pombe* eIF2B map, indicating that the density found in the human structure was the bound ISRIB.

To test these features of ISRIB binding we used CRISPR/Cas9 to randomize residues lining the ISRIB-binding pocket (*Eif2b2*^{N162}, *Eif2b2*^{H188} or *Eif2b2*^{I190}) and correlated amino acid substitutions to ISRIB activity in the mutagenized cells. Histidinol, an agent that activates the eIF2 α kinase GCN2 and induces the ISR, normally activates a CHOP::GFP reporter gene, whilst ISRIB represses the reporter (8). Fluorescence activated cell sorting (FACS) of histidinol-treated, mutagenized cells, segregated them into ISRIB sensitive, ISRIB^{SEN} (CHOP::GFP inhibited), and ISRIB resistant, ISRIB^{RES} (CHOP::GFP activated) classes (Fig. 2A – left and right panels, respectively).

To determine if the phenotypically-distinguished pools of mutagenized cells (Fig. 2A) were enriched in different mutations, we subjected genomic DNA derived from each population to deep sequencing analysis (Fig. 2B & table S4). The ISRIB^{RES} pool targeted at *Eif2b2*^{H188} diverged dramatically from the parental sequence (Fig. 2B, middle panel). Of a total of 250,617 sequencing reads, histidine was present in only 6,443 (2.6%), with arginine, glycine, leucine, lysine and glutamine dominating (24%, 21%, 18%, 8.2% and 6.2%, respectively). Histidine was preserved in the ISRIB^{SEN} pool (269,253 of 328,113 reads, 82%). The ISRIB^{RES} pool of cells targeted at *Eif2b2*^{I190} was dominated by tryptophan, methionine and tyrosine (28%, 24% and 15%, respectively) consistent with a role for these bulky side chains in occluding the ISRIB binding pocket (Fig. 2B – bottom panel). Mutagenesis of *Eif2b2*^{N162} was less successful in generating a pool of strongly ISRIB-resistant cells; nonetheless, threonine was enriched in the ISRIB^{RES} pool

(26%) (Fig. 2B, top panel). Thus, residues lining the ISRIB binding pocket play a role in ISRIB action.

Despite considerable allele diversity, the *Eif2b2*^{H188X} ISRIB^{RES} pool exhibited selective loss of sensitivity to ISRIB, while retaining a measure of responsiveness to certain ISRIB analogs (Fig. 2D). The residual response to analogs AAA1-075B (075B) and AAA1-084 (084) (albeit with much reduced affinity compared to ISRIB^{SEN} population (Fig. 2C), pointed to a shift in the binding properties of the ISRIB pocket, induced by the mutations at β 188.

Next, we exploited the diversity of ISRIB^{RES} mutations in the *Eif2b2*^{H188X} population to select for sub-pools that either acquired sensitivity to compounds AAA1-075B or AAA1-084, regained sensitivity to ISRIB, or retained ISRIB resistance (Fig. 3A) and sequenced their *Eif2b2* alleles (Fig. 3B & table S5). As expected, sorting for ISRIB sensitivity enriched, by over 20-fold, rare wildtype H188 alleles that persisted the ISRIB^{RES} *Eif2b2*^{H188X} pool (Fig. 3B, compare plum and orange bars). H188 was also somewhat enriched in the pools of 075B^{SEN} or 084^{SEN} cells, but unlike the ISRIB^{SEN} these pools were also enriched for residues other than histidine (Fig. 3B & table S5). Importantly, selecting for sensitivity to these ISRIB analogs enriched for different residues than those found in the original ISRIB^{RES} pool: arginine, glycine and leucine were depleted and replaced by lysine, serine, alanine and threonine (Fig. 3B, compare plum to blue and cyan bars). The correlation between mutations in residues lining the ISRIB binding pocket and selective responsiveness to ISRIB analogs, observed in the pools, was confirmed in individual mutant clones (Fig. S5).

To directly address the effect of ISRIB-resistant mutations on ISRIB binding, we purified eIF2B from wildtype, *Eif2b4*^{L180F} and *Eif2b2*^{H188K} CHO cells (Fig. S6). The wildtype eIF2B gave rise to a concentration-dependent FP signal in the presence of a fluorescein-labeled AAA2-101 that was readily competed with unlabeled ISRIB (Fig. 3C). However, eIF2B purified from the mutant cells failed to give rise to an FP signal (Fig. 3D), thereby establishing a correlation between ISRIB resistance in cells and defective ISRIB binding *in vitro*.

The ISRIB binding pocket, defined structurally and validated chemogenetically, straddles the two-fold axis of symmetry of the core regulatory subcomplex, and a single molecule of ISRIB appears to engage the same residues from opposing protomers of the ($\beta\delta$)₂ dimer. These features fit with ISRIB's own symmetry and could explain the ability of ISRIB to stabilize the eIF2B decamer, possibly increasing its abundance in ISRIB-treated cells. Our findings are also consistent with ISRIB's ability to stabilize a rate-limiting assembly intermediate of the active decamer, as demonstrated biochemically in an accompanying manuscript (12). Indeed, comparison of the *S. pombe* (10) and ISRIB-bound human eIF2B speaks against large domain movements associated with ISRIB binding. However, an important allosteric effect of ISRIB binding might easily have been missed, as the critical catalytic domain of the ϵ subunit is resolved in neither structure. Similar considerations apply to the potential effect of ISRIB on the inhibitory interaction between eIF2B with eIF2(α P). These might arise from subtle ISRIB induced conformational changes propagated through the regulatory core to the eIF2(α P) binding cavity formed by the convergence of the tips of the α , β and δ subunits (10, 13-15). The lower resolution of the cryo-EM density in that region might have masked important allosteric changes. Whilst the relative contribution of

accelerated assembly, enhanced stability or allostery to ISRIB action remain to be resolved, it is intriguing to consider that endogenous ligands might engage the ISRIB binding site to regulate eIF2B in yet to be determined physiological states.

References:

1. K. Pakos-Zebrucka *et al.*, The integrated stress response. *EMBO Rep* **17**, 1374-1395 (2016).
2. C. Sidrauski *et al.*, Pharmacological brake-release of mRNA translation enhances cognitive memory. *Elife* **2**, e00498 (2013).
3. M. Halliday *et al.*, Partial restoration of protein synthesis rates by the small molecule ISRIB prevents neurodegeneration without pancreatic toxicity. *Cell Death Dis.* **6**, e1672 (2015).
4. A. Chou *et al.*, Inhibition of the integrated stress response reverses cognitive deficits after traumatic brain injury. *Proc. Natl. Acad. Sci. U. S. A.* **114**, E6420-E6426 (2017).
5. R. Panniers, E. C. Henshaw, A GDP/GTP exchange factor essential for eukaryotic initiation factor 2 cycling in Ehrlich ascites tumor cells and its regulation by eukaryotic initiation factor 2 phosphorylation. *J. Biol. Chem.* **258**, 7928-7934 (1983).
6. J. Siekierka, K. I. Mitsui, S. Ochoa, Mode of action of the heme-controlled translational inhibitor: relationship of eukaryotic initiation factor 2-stimulating protein to translation restoring factor. *Proc. Natl. Acad. Sci. U. S. A.* **78**, 220-223 (1981).
7. M. J. Clemens, V. M. Pain, S. T. Wong, E. C. Henshaw, Phosphorylation inhibits guanine nucleotide exchange on eukaryotic initiation factor 2. *Nature* **296**, 93-95 (1982).
8. Y. Sekine *et al.*, Mutations in a translation initiation factor identify the target of a memory-enhancing compound. *Science* **348**, 1027-1030 (2015).

9. C. Sidrauski *et al.*, Pharmacological dimerization and activation of the exchange factor eIF2B antagonizes the integrated stress response. *Elife* **4**, e07314 (2015).
10. K. Kashiwagi *et al.*, Crystal structure of eukaryotic translation initiation factor 2B. *Nature* **531**, 122-125 (2016).
11. B. R. Hearn *et al.*, Structure-Activity Studies of Bis-O-Arylglycolamides: Inhibitors of the Integrated Stress Response. *ChemMedChem*, (2016).
12. J. Tsai *et al.*, Structure of the nucleotide exchange factor eIF2B reveals mechanism of memory-enhancing molecule. *Science (in press)*, (2018).
13. C. R. Vazquez de Aldana, A. G. Hinnebusch, Mutations in the GCD7 subunit of yeast guanine nucleotide exchange factor eIF-2B overcome the inhibitory effects of phosphorylated eIF-2 on translation initiation. *Mol. Cell. Biol.* **14**, 3208-3222 (1994).
14. G. D. Pavitt, W. Yang, A. G. Hinnebusch, Homologous segments in three subunits of the guanine nucleotide exchange factor eIF2B mediate translational regulation by phosphorylation of eIF2. *Mol. Cell. Biol.* **17**, 1298-1313 (1997).
15. A. M. Bogorad, K. Y. Lin, A. Marintchev, Novel mechanisms of eIF2B action and regulation by eIF2 α phosphorylation. *Nucleic Acids Res.* **45**, 11962-11979 (2017).
16. Y. Sekine *et al.*, Paradoxical Sensitivity to an Integrated Stress Response Blocking Mutation in Vanishing White Matter Cells. *PLoS One* **11**, e0166278 (2016).
17. X. Li *et al.*, Electron counting and beam-induced motion correction enable near-atomic-resolution single-particle cryo-EM. *Nature methods* **10**, 584-590 (2013).
18. K. Zhang, Gctf: Real-time CTF determination and correction. *J. Struct. Biol.* **193**, 1-12 (2016).

19. G. Tang *et al.*, EMAN2: an extensible image processing suite for electron microscopy. *J. Struct. Biol.* **157**, 38-46 (2007).
20. S. H. Scheres, A Bayesian view on cryo-EM structure determination. *J. Mol. Biol.* **415**, 406-418 (2012).
21. S. H. Scheres, RELION: implementation of a Bayesian approach to cryo-EM structure determination. *J. Struct. Biol.* **180**, 519-530 (2012).
22. X. C. Bai, I. S. Fernandez, G. McMullan, S. H. Scheres, Ribosome structures to near-atomic resolution from thirty thousand cryo-EM particles. *Elife* **2**, e00461 (2013).
23. S. H. Scheres, Beam-induced motion correction for sub-megadalton cryo-EM particles. *Elife* **3**, e03665 (2014).
24. S. H. Scheres, S. Chen, Prevention of overfitting in cryo-EM structure determination. *Nature methods* **9**, 853-854 (2012).
25. S. Chen *et al.*, High-resolution noise substitution to measure overfitting and validate resolution in 3D structure determination by single particle electron cryomicroscopy. *Ultramicroscopy* **135**, 24-35 (2013).
26. P. B. Rosenthal, R. Henderson, Optimal determination of particle orientation, absolute hand, and contrast loss in single-particle electron cryomicroscopy. *J. Mol. Biol.* **333**, 721-745 (2003).
27. E. F. Pettersen *et al.*, UCSF Chimera--a visualization system for exploratory research and analysis. *J. Comput. Chem.* **25**, 1605-1612 (2004).
28. P. Emsley, B. Lohkamp, W. G. Scott, K. Cowtan, Features and development of Coot. *Acta Crystallogr. D Biol. Crystallogr.* **66**, 486-501 (2010).

29. P. D. Adams *et al.*, PHENIX: a comprehensive Python-based system for macromolecular structure solution. *Acta Crystallogr. D Biol. Crystallogr.* **66**, 213-221 (2010).
30. T. Burnley, C. M. Palmer, M. Winn, Recent developments in the CCP-EM software suite. *Acta Crystallogr D Struct Biol* **73**, 469-477 (2017).
31. A. Brown *et al.*, Tools for macromolecular model building and refinement into electron cryo-microscopy reconstructions. *Acta Crystallogr. D Biol. Crystallogr.* **71**, 136-153 (2015).
32. R. E. C. Dolle, G-H. Chu. Preparation of pyrrolidinylphenethyl benzoxepine-, tetrahydronaphthalene-, chroman-, and benzofurancarboxamides as κ -opioid agonists. US 2005/54630 A1 (2005).
33. J.B. Carr, Lipogenesis control by esters of benzoxazinecarboxylic acids. U.S. Patent No. 4180572 (1979).

Acknowledgements:

We thank D. Barrett and C. Ortori (University of Nottingham) for measuring the ISRIB content of eIF2B, P. Sterk (University of Cambridge) for NGS analysis, S. Chen, C. Savva, G. McMullan, T. Darling and J. Grimmett (MRC LMB) for technical support with cryo-EM, movie data acquisition and help with computing, S. Preissler (University of Cambridge) for editorial comments and Diamond for access and support of the Cryo-EM facilities at the UK national electron bio-imaging centre (eBIC), (proposals EM-14606 and EM-17057), funded by the Wellcome Trust, MRC and BBSRC.

Funding: A Wellcome Trust Principal Research Fellowship (Wellcome 200848/Z/16/Z) to D.R. A Specialist Programme from Bloodwise (12048), the UK Medical Research

Council (MC_U105161083) and core support from the Wellcome Trust Medical Research Council Cambridge Stem Cell Institute to A.J.W. and a Wellcome Trust Strategic Award to the Cambridge Institute for Medical Research (Wellcome 100140). A Higher Committee for Education Development, Iraq, Scholarship (4241047) to A.A.A.

Author contributions: A.Z. and D.R. designed and implemented the study and wrote the manuscript. F.W., A.F. and A.J.W. obtained and interpreted the structural data and edited the manuscript. A.A.A., C.F. and P.F. designed and synthesized compounds, interpreted the chemogenetic data and edited manuscript. A.C.C., Y.S. and H.P.H. designed and implemented the somatic cell genetics, cell phenotyping and deep sequencing and edited the manuscript. F.A. and L.P. analyzed NGS sequencing data and edited manuscript.

Competing interests: none

Data and materials availability: Cryo-EM density maps are deposited in the Electron Microscopy Data Bank (EMD-4162), and atomic coordinates are deposited in the Protein Data Bank (PDB) (6EZO).

List of Supplementary Materials:

Materials and Methods

Supplementary Text

Fig S1-S6

Table S1-S6

References (16-32)

Figures

Fig. 1

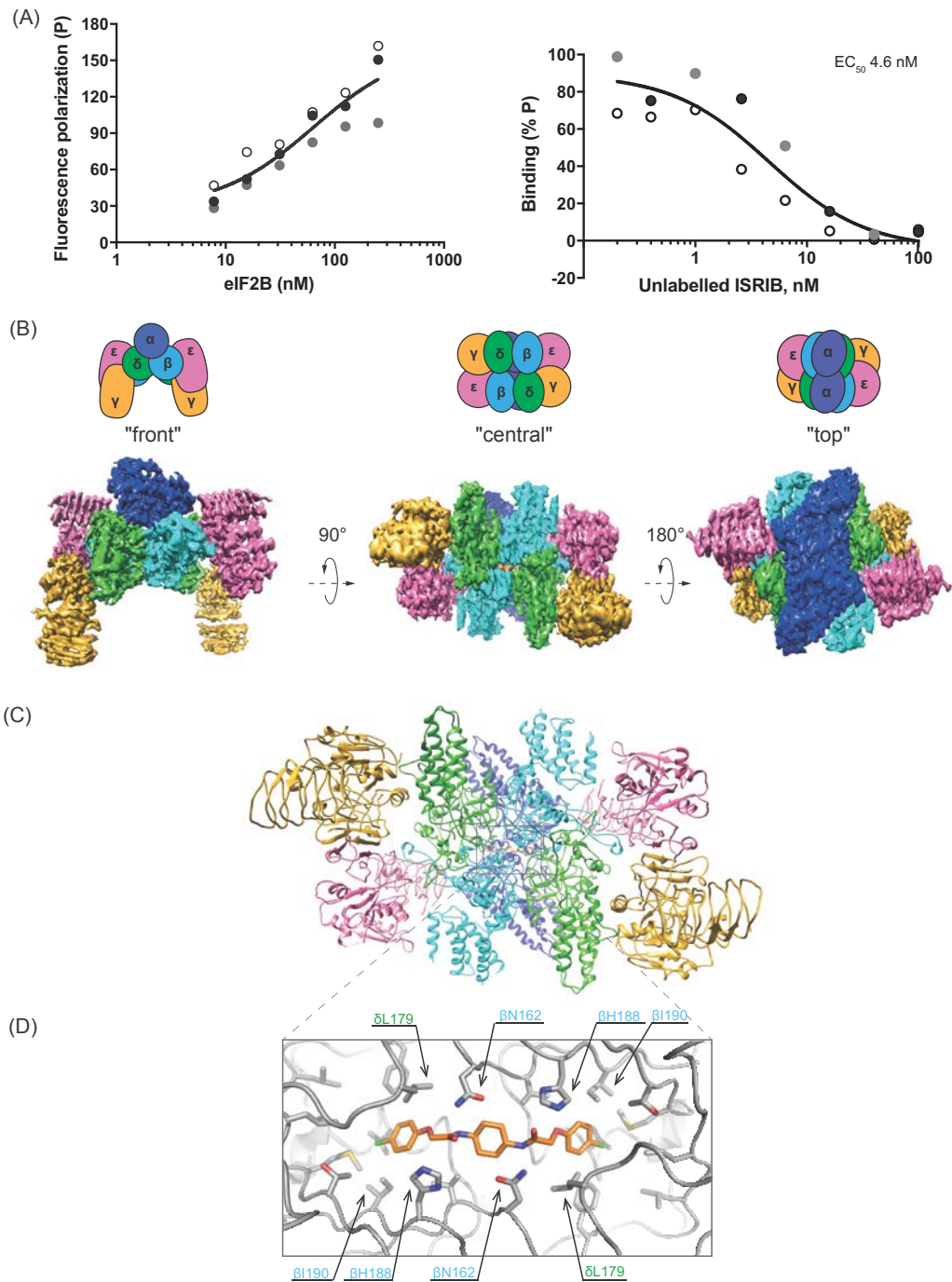


Figure 1***Biophysical and structural analysis of ISRIB binding to human eIF2B***

(A) Fluorescence polarization (FP) assays showing binding of ISRIB to human eIF2B. Left panel: a plot of the FP signal arising from fluorescein-labeled ISRIB analog (AAA2-101) (2.5 nM) as a function of the concentration of eIF2B in the sample. Right panel: a plot of the relative FP signal arising from samples with fluorescein-labeled AAA2-101 (2.5 nM) bound to purified human eIF2B (30 nM) in the presence of the indicated concentration of unlabeled *trans*-ISRIB introduced as a competitor. Concentrations of eIF2B and ISRIB on respective plots are represented on a \log_{10} scale. Curve fitting and EC_{50} was generated using agonist vs. response function on GraphPad Prism, shown are values of three independently-acquired measurements.

(B) Representative views of the cryo-EM map of the ISRIB-bound decameric human eIF2B complex. Density is colored according to the subunit architecture indicated in the cartoons: α – blue, β – cyan, δ – green, γ – gold, ϵ – pink, ISRIB - orange.

(C) Ribbon representation of ISRIB-bound human eIF2B “central” view of the $(\beta\delta)_2$ dimer interface with a single molecule of ISRIB.

(D) Close-up of the “central” view showing the ISRIB binding site. An ISRIB molecule is docked into the cavity at the $(\beta\delta)_2$ dimer interface. Residues contacting ISRIB in the central part of the pocket from the β (blue) and δ (green) subunits are indicated. ISRIB is represented in orange sticks.

Fig. 2

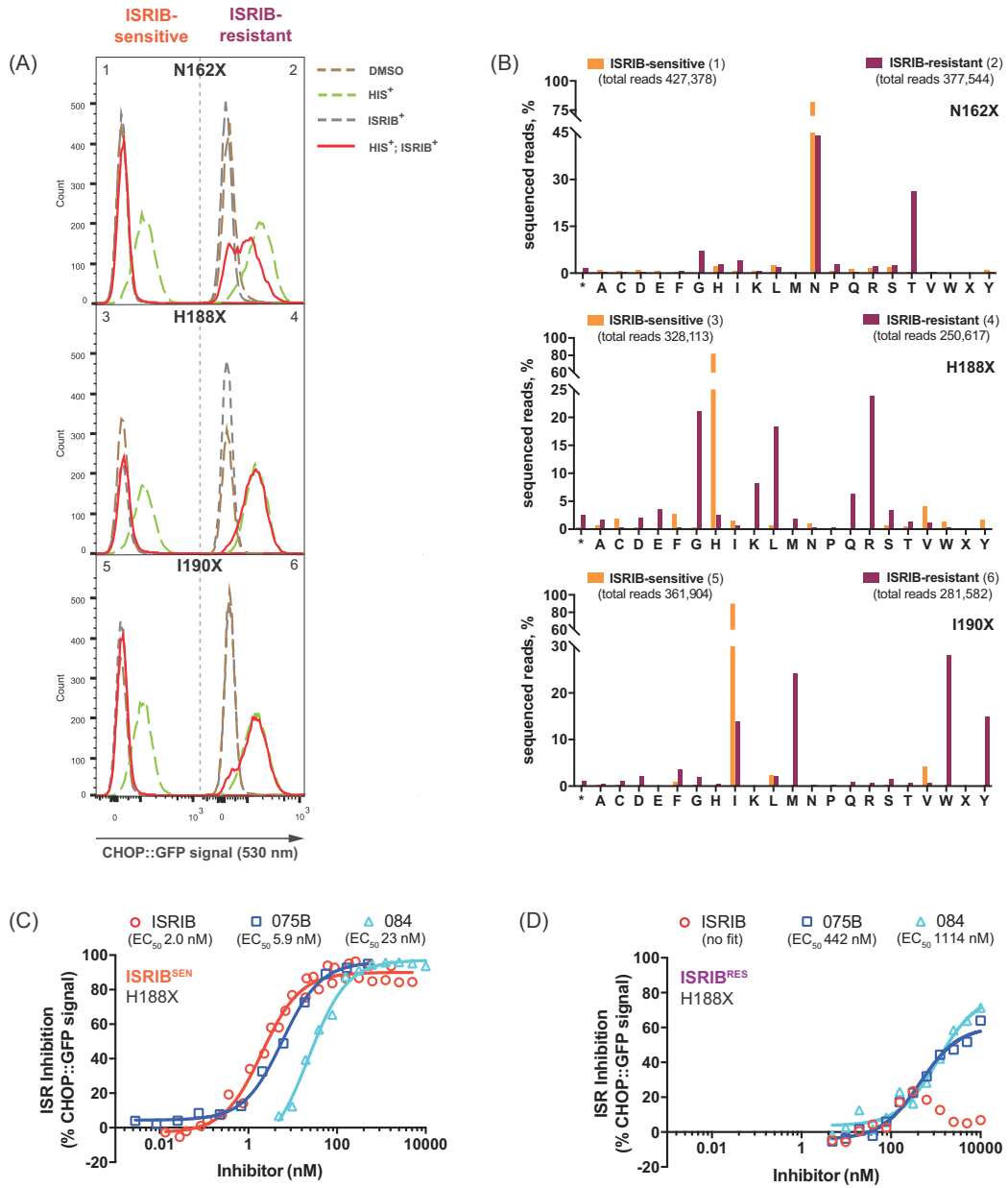


Figure 2

Structure-directed chemogenetic analysis of ISRIB and its analogs' binding to eIF2B.

(A) Histograms of the ISR-responsive CHOP::GFP fluorescent reporter activity, induced by histidinol (HIS^+ , 0.5 mM) in ISRIB-sensitive (ISRIB^{SEN}) (left panels) and ISRIB-resistant (ISRIB^{RES}) (right panels) pools of CHO-K1 cells, selected for their responsiveness to ISRIB (200 nM), following CRISPR/Cas9-induced random mutagenesis of the indicated codon of *Eif2b2*.

(B) Bar graph of the distribution of residues identified at the indicated positions of mutagenized *Eif2b2*, analyzed by the next generation sequencing (NGS). Shown is the number of sequenced reads in ISRIB^{SEN} pools (orange bars) or ISRIB^{RES} pools (plum bars) encoding each amino acid (* - stop codon, X – ambiguous sequence).

(C) Graphs showing inhibition of the ISR-activated CHOP::GFP reporter (induced as in panel “A”) by ISRIB or two related analogs, compound AAA1-075B (075B) and compound AAA1-084 (084), in ISRIB^{SEN} (left) and ISRIB^{RES} (right) mutant pools of *Eif2b2*^{H188X}. Shown is a representative from three independent experiments for each of the compounds. Concentration of inhibitor is represented on a \log_{10} scale. Curve fitting and EC_{50} was generated using agonist vs. response function on GraphPad Prism.

Fig. 3

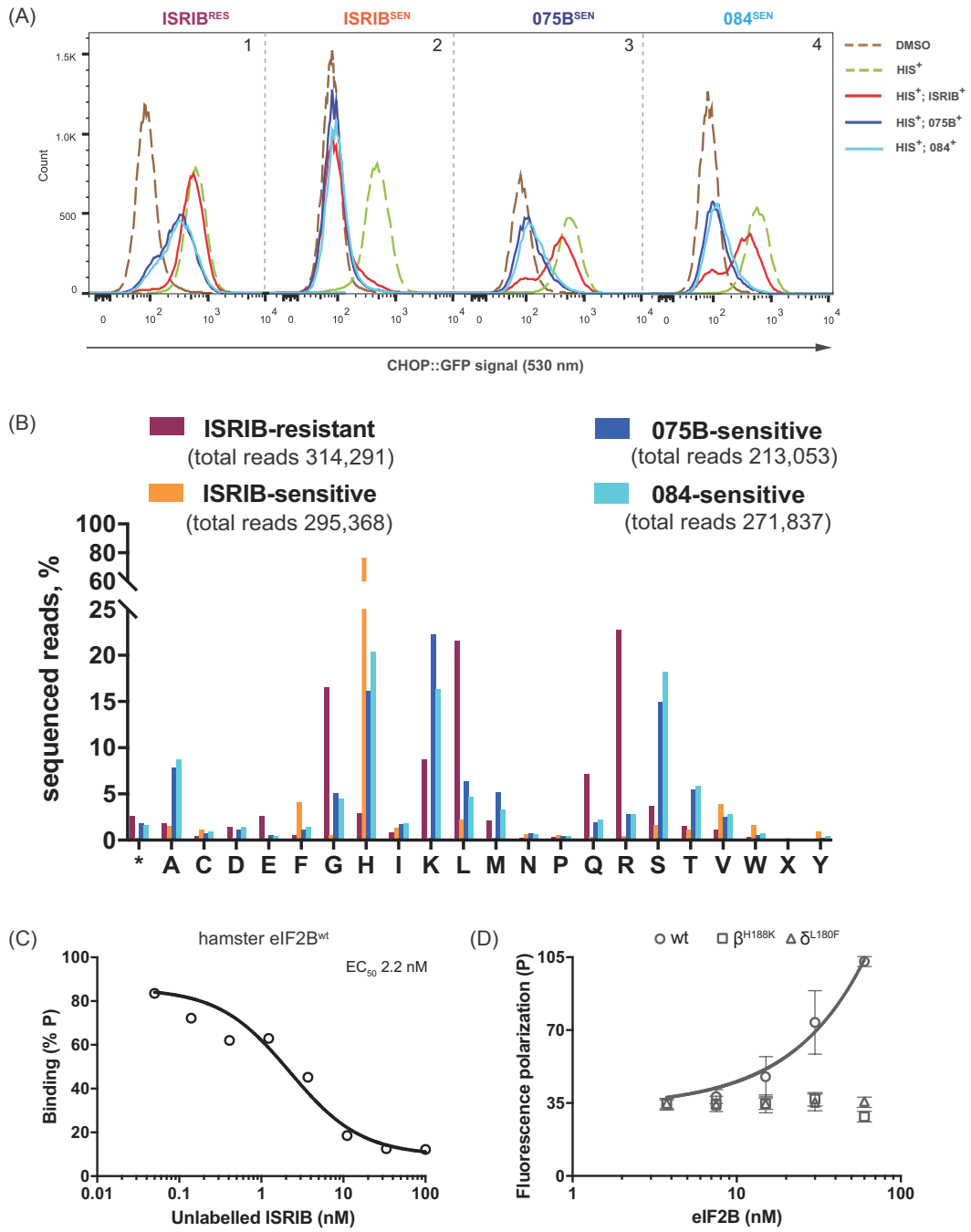


Figure 3***Sensitivity to ISRIB analogs selects for a divergent palette of mutations in codon 188 of Eif2b2***

(A) Histograms of the ISR-responsive CHOP::GFP fluorescent reporter activity, induced by histidinol (HIS+, 0.5 mM) in ISRIB^{RES}, ISRIB^{SEN}, compound 075B^{SEN} and compound 084^{SEN} sub-pools, selected for their responsiveness to ISRIB or its analogs (2.5 μM) from a population of originally ISRIB^{RES} *Eif2b2*^{H188X} mutant cells.

(B) Bar graph of the distribution of residues identified at *Eif2b2* codon 188 in phenotypically divergent pools of CHO-K1 cells. The number of sequenced reads in ISRIB^{RES} (plum), ISRIB^{SEN} (orange), compound 075B^{SEN} (blue) and compound 084^{SEN} (cyan) pools encoding each amino acid (* - stop codon, X – ambiguous) is plotted.

(C) Plot of the relative FP signal arising from samples with fluorescein-labeled AAA2-101 (2.5 nM) bound to purified hamster eIF2B (30 nM) in the presence of the indicated concentration of unlabeled ISRIB introduced as a competitor (represented on a log₁₀ scale). Shown is a representative of two independent experiments. The fitting curve and EC₅₀ was generated using “agonist vs. response” function on GraphPad Prism.

(D) A plot of the FP signal arising from fluorescein-labeled AAA2-101 (2.5 nM) as a function of the concentration of wildtype (wt) or mutant eIF2B (δ^{L180F} or β^{H188K}) in the sample. Shown are mean ± SD (n=3). Concentrations of eIF2B are represented on a log₁₀ scale.



Supplementary Materials for

Binding of the integrated stress response inhibitor, ISRIB, reveals a regulatory site in the nucleotide exchange factor, eIF2B

Alisa F. Zyryanova¹, Félix Weis^{1-4,†}, Alexandre Faille^{1-3,†}, Akeel Abo Alard⁵, Ana Crespillo-Casado¹, Yusuke Sekine¹, Heather P. Harding¹, Felicity Allen⁶, Leopold Parts⁶, Christophe Fromont⁵, Peter M. Fischer⁵, Alan J. Warren^{1-4,*} and David Ron^{1,*}

correspondence to: dr360@medschl.cam.ac.uk, az310@cam.ac.uk,
ajw1000@cam.ac.uk

This PDF file includes:

Materials and Methods
Scheme S1 to S4
Figs. S1 to S6
Tables S1 to S6

Materials and Methods

Cell culturing and reagents

The HeLa-derived cell line was maintained in DMEM Joklik modification (M0518, Sigma) supplemented with 0.2% NaHCO₃ (S8761, Sigma), Newborn Calf Serum (N4637, Sigma), 1x Penicillin/Streptomycin (P0781, Sigma), 1x non-essential amino acid solution (M7145, Sigma), and 55 μM β-mercaptoethanol. Suspension cultures were grown in either Erlenmeyer flasks in a Minitron shaker (Infors HT) at a shaking speed 70 rpm, 37°C, 8% CO₂, or in a Cellbag (BC10, GE Healthcare) using a WAVE Bioreactor 20/50 EHT system (GE Healthcare) at 37°C, 8% CO₂, air flow 0.3 sp, angle 5°-7.5°, rotation speed 15-18.5 rpm.

CHO-K1-derived cell lines were maintained either in Nutrient Mixture F12 (N4888, Sigma), 10% Fetal Calf serum (FetalClone II, Thermo), 2 mM L-glutamine, and 1x Penicillin/Streptomycin at 37°C with 5% CO₂ for adherent cells or in MEM Alpha (M8042, Sigma) with 10% Fetal Calf serum, 2 mM L-glutamine, 1x Penicillin/Streptomycin, 1x non-essential amino acid solution, and 55 μM β-mercaptoethanol in Erlenmeyer flasks in Minitron shaker (Infors HT) at a shaking speed 70 rpm, 37°C, 8% CO₂ for suspension cells.

Sucrose Gradient

75x10⁶ cells (in 75 mL) of HeLa-2C2 (3xFLAG-*EIF2B2* in/in) cell suspension were treated for 20 minutes with either 150 μL DMSO or 200 nM ISRIB, prior to harvesting and lysing in 3x cell pellet volume of the lysis buffer [50 mM Tris (pH 7.4), 400 mM KCl, 4 mM Mg(OAc)₂, 0.5% Triton, 5% Sucrose, 1 mM DTT, 2 mM PMSF, 10 μg/ml Aprotinin, 4 μg/μl Pepstatin, 4 μM Leupeptin]. Lysates were cleared at 21,130 g in a chilled centrifuge, 0.5 mL of the supernatant was applied on 5mL of 5-20% Sucrose gradient, that was prepared on SG15 Hoeffler Gradient maker in the cell lysis buffer with respective amounts of sucrose and equilibrated for 24 hours on ice. Velocity gradient centrifugation was on a SW50.1 rotor at 40,000 rpm for 14 hours and 20 minutes and the gradient was divided into 13 fractions of 420 μL. Each fraction was then diluted two-fold with lysis buffer without sucrose, proteins were precipitated with 20% TCA for 16 hours at 4°C and pelleted at 21,130 g for 20 minutes in a chilled centrifuge. Protein pellets were washed twice with ice-cold acetone, air-dried, resuspended in 60 μL of alkaline SDS loading buffer and 5 μL of resuspension was resolved on a 12.5% SDS-PAGE gel. The protein gel was then transferred onto PVDF membrane and immunoblotted, using primary monoclonal mouse anti-FLAG M2 antibody (F1804, Sigma) and secondary polyclonal goat anti-mouse-IR800, followed by scanning on Odyssey imager (LI-COR Biosciences) and image analysis on ImageJ software.

Protein purification

Human eIF2B was purified from 50 L of HeLa-2C2 cells (3xFLAG-*EIF2B2* in/in) grown in suspension at a maximum density of 10⁶ cells/mL. Cell pellets (150 grams total) were harvested at room temperature and washed twice with room temperature PBS. Cells were then lysed in 2 pellet volumes of lysis buffer [50 mM Tris (pH 7.4), 150 mM NaCl, 0.5% Triton, 10% Glycerol, 5 mM MgCl₂, 1 mM DTT, 2 mM PMSF, 10 μg/ml Aprotinin, 4 μg/μL, Pepstatin, 4 μM Leupeptin]. For

structural analysis lysis buffer was supplemented with 200 nM ISRIB. Lysates were cleared at 20,000 rpm (JA 25.50) at 4°C and supernatants were incubated with 5 mL of anti-FLAG M2 affinity gel (A2220, Sigma) for one hour at 4°C. The resin with bound eIF2B was washed three times for 5 minutes with 10 mL of ice-cold lysis buffer containing 500 mM NaCl, then washed three times for 5 minutes with 10 mL of washing buffer [50 mM Tris (pH 7.4), 150 mM NaCl, 0.1% CHAPS, 5m M MgCl₂, 1 mM DTT]. The bound protein was eluted twice sequentially in 10 mL of the washing buffer supplemented with 150 mg/mL 3X FLAG peptide (F4799, Sigma), concentrated to 2 mg/mL using 100K MWCO PES concentrator (88503, Pierce) and 100 µL of concentrated protein complex was size fractionated on a SEC-3 300 Å HPLC column (P.N. 5190-2513, Agilent) at a flow rate of 0.35 mL/min in gel filtration buffer [50 mM Tris (pH 7.4), 150 mM NaCl, 5 mM MgCl₂, 1 mM DTT]. The centre of the 280 nm absorbance peak eluting around 6 minutes was collected in 42 µL and then applied onto cryo-grids for subsequent cryo-electron microscopy imaging. For the fluorescence polarization experiments the concentrated FLAG-M2 eluate was used.

Hamster eIF2B from CHO-S7 [*Eif2b3*-3xFLAG in/in; *Eif2b4*^{wt}], CHO-S9 [*Eif2b3*-3xFLAG in/in; *Eif2b4*^{L180F} in/Δ] or CHO-B3 [*Eif2b3*-3xFLAG in/in; *Eif2b2*^{H188K} in/ Δ] was purified as human eIF2B (above) (16), with following modifications: Hamster eIF2B^{wt} cells were harvested from 3.5 L of CHO-S7 suspension culture grown at maximum density of 10⁶ cells/mL, washed with room temperature PBS and lysed in two pellet volumes of lysis buffer. Cleared lysate supernatant was incubated with 300 µL of anti-FLAG M2 affinity gel. The resin was washed three times for 5 minutes with 1 mL of lysis buffer containing 500 mM NaCl, then washed three times for 5 minutes with 1 mL of washing buffer [50 mM Tris (pH7.4), 150 mM NaCl, 2 mM MgCl₂, 0.01% Triton, 1 mM DTT]. Protein was eluted in two resin volumes of washing buffer supplemented with 125 mg/mL 3X FLAG peptide. Hamster eIF2B^{ΔL180F} along with eIF2B^{βH188K} mutant cells (with total cell count of 50x10⁷ each) were harvested and washed with room temperature PBS, then lysed in three pellet volumes of lysis buffer. Cleared lysate supernatant was incubated with 60 µL of anti-FLAG M2 affinity gel following binding, washing and eluting procedures as described above.

Fluorescence polarization assay

20 µL reactions were assembled in 384-well round bottom polystyrene plates (3677, Corning), equilibrated in the assay buffer [50 mM Tris (pH7.4), 150 mM NaCl, 2 mM MgCl₂, 0.01% Triton, 1 mM DTT] for 10 minutes at room temperature and either read directly or read 25 minutes after addition of unlabeled competitor on a CLARIOstar microplate reader (BMG Labtech) with filter settings of 482 nm (excitation) and 530 nm (emission). The fluorescein-labeled AAA2-101 compound was used in the range of 1-100 nM with corresponding amounts of purified eIF2B of 30-250 nM. Each measurement point was either an average of six readings every 30 seconds (for eIF2B dose-response) or five readings every 60 seconds (for unlabeled competitor assay).

Binding of the fluorescent probe to eIF2B in the competition experiments was expressed as a fraction of relative polarization signal (%P) over the dynamic range of the assay. Relative polarization was calculated by subtracting background FP (P_{bg}) from experimental FP (P_{ex}) ($P = P_{ex} - P_{bg}$). The minimal FP (P_{min}) observed when no

eIF2B was added and the maximal FP (P_{\max}) with eIF2B alone (in the presence of probe and in absence of non-fluorescent competitor compounds) define the dynamic range of the assay. Values of relative polarization for any assay point ($\%P_n$) were calculated using the formula $\%P_n = (P_n - P_{\min}) / (P_{\max} - P_{\min}) * 100$.

Measuring ISRIB action in cultured cells:

ISRIB action was tracked by its effects on the activity of a stably-integrated ISR-responsive CHOP::GFP reporter gene in CHO-K1 cells, as described previously (8). Inhibition of histidyl-tRNA synthetase by histidinol activates the eIF2 α kinase GCN2 that phosphorylates eIF2. eIF2(α P) inhibits the GEF eIF2B, initiating the ISR and culminating in CHOP::GFP activation, which is detected by fluorescent activated cell sorting (FACS). In wildtype, ISRIB-sensitive cells the presence of ISRIB attenuates the response of the CHOP::GFP reporter, whereas in ISRIB resistant, mutant cells, the CHOP::GFP reporter remains active despite ISRIB's presence.

40 x 10³ CHO-K1 derivatives carrying a stable CHOP::GFP reporter transgene were plated in 6 well plates. Two days later the culture medium was replaced with 2 mL of fresh medium and compounds added. Immediately before analysis, the cells were washed with PBS and collected in PBS containing 4 mM EDTA. Single cell fluorescent signals (10,000/sample) measured by FACS Calibur (Beckton Dickinson). FlowJo software was used to analyze the data.

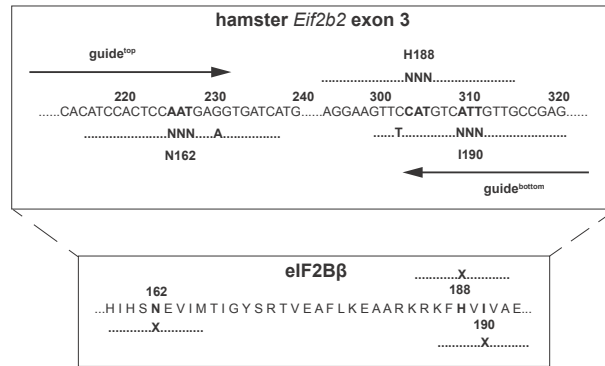
Generation of the genome edited cells with altered ISRIB responsiveness by CRISPR/Cas9

The genotypes and descriptions of the cell lines is provided in [table S1](#).

Cell lines HeLa-2C2 cells [3xFLAG-EIF2B2 in/in] and CHO-S7 [*Eif2b3*-3xFLAG in/+; *Eif2b4*^{wt}] have been previously described (8, 16).

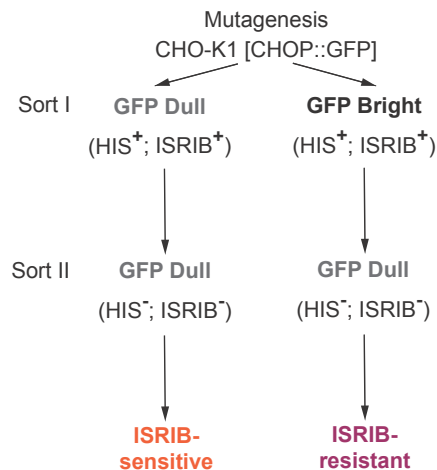
To generate CHO-S9 [*Eif2b3*-3xFLAG in/in; *Eif2b4*^{L180F} in/ Δ] a 3xFLAG tag was incorporated into the *Eif2b3* gene of CHO-C30 [*Eif2b4*^{L180F} in/ Δ] cells at the C-terminus of eIF2B γ subunit by a CRISPR/Cas9 mediated homology-directed repair following a published procedure (16). In brief, CHO-C30 [*Eif2b4*^{L180F} in/ Δ] cells were plated in 6-well plates at a density of 2 x 10⁵ per well. 24 hours later the cells were transfected with the repair template plasmid (1 μ g) and an sgRNA/Cas9 plasmid (1 μ g) using Lipofectamine LTX (Invitrogen) according to manufacturer's instruction. The next day, GFP positive cells, which indicate plasmid-transfected cells, were collected using a Beckman Coulter MoFlo Cell sorter, and expanded as single clones in 96 well plates. Genomic DNAs isolated from the clones were screened and sequenced to confirm the insertion. Cells from clone S9 were then used to purify endogenous γ -3xFLAG-tagged eIF2B.

Site-directed random mutagenesis of hamster *Eif2b2* was carried out using CRISPR/Cas9 homologous repair using an equimolar mixture of single-stranded oligo deoxynucleotides (ssODN) as repair templates containing combination of all possible codons (n=64) for each targeted site proving the diversity of substitutions ([Scheme S1](#)). Each set of ssODNs was transfected along with a sgRNA guide, inserted into a vector containing mCherry marked Cas9, in the following pairs: UK2105 with ssODN-1922 or ssODN-1923, UK2106 with ssODN-1924 (see [tables S2, S3](#) for further description of repair templates and guide vectors (UK2105, UK2106).



Scheme S1. CRISPR/Cas9 directed mutagenesis of the hamster *Eif2b2* gene at the locus encoding ISRIB contact sites on the eIF2B β subunit revealed by the structure: N162, H188 or I190. Hamster *Eif2b2* exon 3 with the two RNA guides, directing Cas9 to mediate double strand break, and the aligned single-strand repair templates. The randomized substitution of the original codon is indicated (NNN), as are the silent PAM-disrupting mutations. Nucleotide numbering corresponds to GeneBank accession NW_003613913.1.

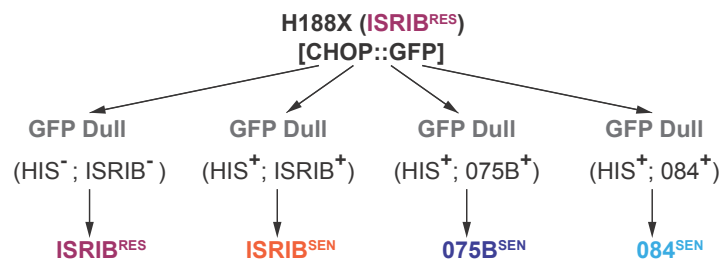
For transfection 20×10^3 CHO-S7 cells (derivatives of CHO-K1 bearing 3xFLAG-tagged *Eif2b3*) (16) were plated 36 hours prior being transfected with equal amounts of $1 \mu\text{g}$ guide and $1 \mu\text{g}$ ssODN using standard Lipofectamine protocol, expanded and sorted 48 hours later (Scheme S2). Before sorting for ISRIB resistance or sensitivity a technical “mCherry-positive” sort for successfully transfected cells was done and 240K, 360K and 330K cells were collected for N162X, H188X and I190X templates respectively. Five days later the recovered cell pools were treated with 0.5 mM histidinol (22883, Acros) and 200 nM ISRIB. 20 hours later pools were sorted for “GFP-bright” (ISRIB-resistant) and “GFP-dull” (ISRIB-sensitive) phenotypes (Sort I, scheme S2). 37K, 126K and 240K cells for each of respective ISRIB-resistant pools: N162X, H188X and I190X, and 500K for each of ISRIB-sensitive pools were collected. 10 days later “GFP-dull” sort of untreated pools (Sort II, scheme S2) was carried out, to eliminate clones with a constitutively active ISR. 1×10^6 cells were collected for each of ISRIB-resistant and ISRIB-sensitive pools.



Scheme S2. Selection of ISRIB-sensitive (ISRIB^{SEN}) and ISRIB-resistant (ISRIB^{RES}) cells (Sort I) and elimination of cells with constitutive ISR (Sort II) following

CRISPR/Cas9 mutagenesis, based on the ISR-activated CHOP::GFP fluorescent reporter upon histidinol (HIS) treatment of CHO-K1 cells.

For a new round of sorting to reselect analog-sensitive pools from ISRIB-resistant *Eif2b*^{H188X} pool (Scheme S3), 1 x 10⁶ cells were plated 36 hours before being treated with 0.5 mM histidinol and 2.5 μM of ISRIB or 2.5 μM ISRIB analog (AAA1-075B or AAA1-084). 20 hours later cells were sorted for “GFP-dull” (analog-sensitive) phenotype, and 1 x 10⁶ cells were collected for each respective pool (ISRIB-sensitive, 075B-sensitive and 084-sensitive). Note that a newly selected ISRIB-resistant pool that did not undergo any treatments prior being sorted, serving as a control population.



Scheme S3. Selection of ISRIB^{RES}, ISRIB^{SEN}, AAA1-075B sensitive (075B^{SEN}) and AAA1-084 sensitive (084^{SEN}) cells, based on the ISR-activated CHOP::GFP fluorescent reporter upon histidinol (HIS) treatment in *Eif2b2*^{H188X} mutant population.

Cell pools were then expanded, phenotypically characterized and their genomic DNA obtained for subsequent next-generation sequencing analysis. Individual clones were genotyped following Sanger sequencing of PCR products amplified from genomic DNA.

All cells were washed with PBS once and collected in PBS containing 4 mM EDTA and 0.5% BSA and sorted on INFLUX cell sorter.

NGS sequencing of *Eif2b2* containing targeted mutations

Genomic DNA was prepared from 1 x 10⁷ cells using Blood and Cell culture Midi Kit (13343, Qiagen). Then two rounds of PCR were performed to isolate amplicons for NGS sequencing. The first round of 18 cycles with primers 1975 and 1976 to amplify a 244 bp region of *Eif2b2* from 31 μg of DNA (corresponding to genomic DNA from 19,300 cells) divided into 5 PCR reactions of 50 μL using Q5 polymerase (M0493, NEB) according to the manufacturer’s protocol. The PCR reactions were then pooled together and combined with 250 μL of solubilization buffer from Gene-Jet gel purification kit (K0691, Thermo Fisher). Thereafter mixes were purified following the standard Gene-Jet gel purification protocol (without adding the isopropanol recommended for smaller products). The second round used 11-15 cycles of PCR with a universal Illumina P5 primer (1977) and individually barcoded P7 primers for each sample (1762-1768). The resulting products were purified as above and quantified using Agilent DNA chip 1000 and qPCR with Illumina P5 and P7 primers and subject to Illumina SE150bp NGS sequencing (Figure

2B and table S4) or SE50 NGS sequencing (Figure 3B and table S5). Primers details are provided in Table S2).

The sequencing reads were converted to BAM files aligned to the hamster EIF2b2 locus and then corresponding SAM files were aligned to 31 bp templates surrounding each mutation: N162 (NNGAXGTGATCATGACCATGGCTATTCT), H188 (CGAAAGAGGAAGTTCNNNGTCATTGTTGCC) and I190 (CGAAAGAGGAXGTTXCATGTCNNNGTTGCCS). Reads that differed by less than three residues outside the degenerate sequence were counted for codons and amino acids at each position using Python scripts.

Electron microscopy

3 μ L aliquots of the protein complex diluted to 2 μ M in gel filtration buffer were applied on holey carbon grids (Quantifoil 300 mesh R2/2), rendered more hydrophilic with a 20 seconds 9:1 argon–oxygen plasma treatment (Fischione Model 1070). Grids were blotted and flash-frozen in liquid ethane using a Vitrobot mark II (Thermo Fisher) with a blotting time of 7s at 10 °C and 100% humidity. Data acquisition was performed on a Titan Krios microscope (Thermo Fisher) operated at 300 kV. The dataset was recorded on a back-thinned Falcon II detector (Thermo Fisher) at a calibrated magnification of x 80 000 (resulting in a pixel size of 1.75 Å on the object scale) with a defocus range of 2.5–3.5 μ m. An in-house built system was used to intercept the videos from the detector at a speed of 25 frames for the 1.5 second exposures. Data were acquired automatically using the EPU software (Thermo Fisher).

Image processing

After visual inspection of the micrographs, 765 images were selected for further processing. The movie frames were aligned with MotionCorr (17) for whole-image motion correction. Contrast transfer function parameters for the micrographs were estimated using Gctf (18). 237,486 particles were selected semi-automatically using the e2boxer routine from EMAN2 (19). All 2D and 3D classifications and refinements were performed using RELION (20, 21).

Reference-free 2D classification (Fig. S3A) was first performed, followed by a 3D classification step using a low-pass filtered (60 Å) map calculated from the tetrameric eIF2B ($\beta\delta$)₂ complex from *Chaetomium thermophilum* (PDB: 5DBO). An initial map was consistent with the presence of all five subunits in our sample and also the existence of C2 symmetry. We subclassified particles into 8 3D classes (Fig. S3B). One class representing 17 % of the dataset (41750 particles) was then used for 3D refinement in C2 symmetry.

Statistical movie processing was performed as described (22), including modelling of the fall-off of high-resolution information content by radiation damage in a dose-dependent manner as described (23). The reported overall resolution of 4.1 Å was calculated using the gold-standard Fourier shell correlation (FSC) 0.143 criterion (24) (Fig. S3C) and was corrected for the effects of a soft mask on the FSC curve using high-resolution noise substitution (25) (Fig. S3E). The final density map

was corrected for the modulation transfer function of the detector and sharpened by applying a negative B factor that was estimated using automated procedures (26).

As a control experiment, data were also processed without applying symmetry (C1). This generated a map at 4.2 Å resolution that still contained a density attributable to ISRIB in the core of the complex (data not shown).

Model building and refinement

S. pombe eIF2B structure (PDB accession code: 5B04, (10)) was used as a starting model. A poly-alanine (glycines were immediately added to account for flexibility) model was generated and subunits were individually fitted to the density map in Chimera (27). This model was then finely fitted using real space refinement and loops found to be divergent between *S. pombe* and human were rebuilt in Coot (28). All side chains for which density was clearly resolved (up to 37% of non-Ala non-Gly residues in α and β subunits and as low as 8% in ϵ subunits) were positioned. The ISRIB molecule was then manually fitted in the density located at the regulatory core of eIF2B.

The model was then refined using phenix.real_space_refine (29) to optimize both protein and ligand geometry and limit clashes. Finally, REFMAC in CCP-EM (30) was used to further refine the model and automatically generate the map vs. model FSC curves (Fig. S3D) and assess overfitting, as described (31). Briefly, the procedure involved initial random displacement of the atoms within the final model and refinement against one of the two half maps to generate the FSC_{work} curve. A cross-validated FSC_{free} curve was then calculated between this refined model and the other half map. The similarity between FSC_{work} and FSC_{free} curves is indicative of the absence of overfitting. Maps were analyzed and visualized using Chimera (27). Figures were prepared using Chimera and Pymol (Molecular Graphics System, Version 2.0.6 Schrödinger, LLC, <http://www.pymol.org>).

Information on structural data processing is summarized in table S6.

ISRIB analogs chemistry

Compound design (Scheme S4). To observe ISRIB's interaction with eIF2B directly, we designed a fluorescently labeled derivative (AAA2-101) (Fig. S2A) based on known structure–activity relationships of ISRIB derivatives (11). These show that major modifications of the central *trans*-cyclohexyl group and the glycolamide linkages are poorly tolerated, whereas changes to the terminal aryl groups in some cases maintain or enhance activity. Since conservative modifications of the glycolamide portions appeared possible (11), we attempted to tether the glycolamide C ^{α} of one of the cyclohexyl substituents to the neighboring phenyl in the form of a chromane group. We observed that the compound containing this group (AAA1-084, Fig. S2A) retained activity and was only 8.5-fold less active than *trans*-ISRIB (Fig. S2B). Molecular modeling (compare (10); Figure 3C therein) suggested that the benzylic C of the chromane system would face the solvent-accessible entry into the putative ISRIB-binding site of eIF2B. Replacement of the chromane with the dihydrobenzoxazine system afforded a compound (AAA1-075B, Fig. S2A) only 3-fold less active than *trans*-ISRIB (Fig. S2B). The aniline function in this compound

was then used to elaborate the fluorescently labeled compound AAA2-101, which contains a flexible linker terminating in a 5/6-carboxyfluorescein moiety.

General. LC-MS analyses were performed using a Shimadzu UFLCXR system coupled to an Applied Biosystems API2000 mass spectrometer. The HPLC column used was Phenomenex Gemini-NX, 3 μ m-110 Å, C₁₈, 50 x 2 mm with a flow rate of 0.5 mL/min and UV monitoring at 220 and 254 nm. Gradient elution: pre-equilibration for 1 min at 5% eluant B in eluant A; then 5 to 98% B over 2 min, 98% B for 2 min, 98 to 10% B over 0.5 min, then 10% B for one min. Eluant A: 0.1% HCOOH in H₂O; eluant B: 0.1% HCOOH in MeCN. ¹H-NMR spectra were recorded using a Bruker-AV 400 instrument operating at 400.13 MHz and ¹³C-NMR spectra were recorded at 101.62 MHz. Chemical shifts (δ) are in parts per million (ppm) with reference to solvent chemical shift. High-resolution time-of-flight electrospray (TOF-ES⁺) mass spectra (HR-MS) were recorded using a Bruker micrOTOF spectrometer.

***N,N'*-((1*r*,4*r*)-Cyclohexane-1,4-diyl)bis(2-(4-chlorophenoxy)acetamide) (2a; trans-ISRIB).** This compound was prepared from *trans*-1,4-cyclohexanediamine (**1a**) and 4-chlorophenoxyacetyl chloride as described (2). ¹H-NMR (DMSO-*d*₆): δ 7.97 (d, *J* = 8.0 Hz, 2H), 7.33 (d, *J* = 8.8 Hz, 4H), 6.96 (d, *J* = 8.6 Hz, 4H), 4.44 (s, 4H), 3.58 (br s, 2H), 1.75 (br d, *J* = 7.5 Hz, 4H), 1.33 (quint, *J* = 10.2 Hz, 4H); ¹³C-NMR (DMSO-*d*₆): δ 167, 157, 129, 125, 117, 67, 47, 31; LC-MS: *m/z* 451.3 [M + H]⁺; HPLC: *t*_R 2.92 min (> 95%).

***N,N'*-((1*s*,4*s*)-Cyclohexane-1,4-diyl)bis(2-(4-chlorophenoxy)acetamide) (2b; cis-ISRIB).** This compound was prepared from *cis*-1,4-cyclohexanediamine (**1b**) and 4-chlorophenoxyacetyl chloride as described (2). ¹H-NMR (DMSO-*d*₆): δ 7.87 (d, *J* = 7.1 Hz, 2H), 7.34 (d, *J* = 9.5 Hz, 4H), 6.98 (d, *J* = 8.7 Hz, 4H), 4.49 (s, 4H), 3.73 (br s, 2H), 1.54-1.63 (m, 8H); ¹³C-NMR (DMSO-*d*₆): δ 167, 157, 130, 125, 117, 67, 45, 28; LC-MS: *m/z* 451.4 [M + H]⁺; HPLC: *t*_R 2.96 min (95%).

***N,N'*-((1*r*,4*r*)-Cyclohexane-1,4-diyl)bis(2-methoxyacetamide) (3; AAA1-090).** A stirred solution of **1a** (0.11 g, 1 mmol) and iPr₂NEt (0.37 mL, 2.2 mmol) in CH₂Cl₂ (5 mL) was cooled to 0 °C. Methoxyacetyl chloride (0.19 mL, 2.2 mmol) in CH₂Cl₂ (1 mL) was added dropwise. The resulting suspension was stirred at 0 °C for 30 min and at room temperature for 1 h. EtOAc was added and the solution was extracted successively with saturated aq solutions of NH₄Cl, NaHCO₃, and brine. The organic phase was dried with Na₂SO₄, filtered, and evaporated. The residue was triturated with Et₂O, collected and dried to afford the title compound as a white powder (0.219 g, 85%) ¹H-NMR (DMSO-*d*₆): δ 7.55 (d, *J* = 8.8 Hz, 2H), 3.75 (s, 4H), 3.55 (br s, 2H), 3.28 (s, 6H), 1.70 (d, *J* = 8.4 Hz, 4H), 1.33 (quint, *J* = 19.7 Hz, 4H); ¹³C-NMR (DMSO-*d*₆): δ 168, 72, 59, 47, 31; HR-MS: *m/z* 259.1660 [M + H]⁺, C₁₂H₂₃N₂O₄ requires 259.1652.

***N*-((1*r*,4*r*)-4-Aminocyclohexyl)-2-(4-chlorophenoxy)acetamide (4b).** A stirred solution of *tert*-butyl ((1*r*,4*r*)-4-aminocyclohexyl)carbamate (**1c**, 2.143 g, 10 mmol) and iPr₂NEt (1.9 mL, 11 mmol) in CH₂Cl₂ (50 mL) was cooled to 0 °C (ice bath). 4-Chlorophenoxyacetyl chloride (1.7 mL, 11 mmol) in CH₂Cl₂ (3 mL) was added dropwise. The resulting suspension was stirred at 0 °C for 30 min and at room temperature for 1 h. EtOAc was added and the solution was extracted successively with saturated aq solutions of NH₄Cl, NaHCO₃, and brine. The organic phase was dried with Na₂SO₄, filtered, and evaporated. The residue was triturated with Et₂O, collected, and dried to afford the Boc-protected intermediate **4a** as a white powder (3.63 g, 95%).

A suspension of **4a** (1.43 g, 3.5 mmol) in dioxane–MeOH (2:1; 6 mL) was treated with 4 M HCl in dioxane (7 mL, 28 mmol) with stirring for 2 h. The resulting solution was evaporated and the residue was triturated with Et₂O, collected, and dried to afford the HCl salt of the title compound **4b** as a white powder (1.071 g, 96%). ¹H-NMR (DMSO-*d*₆): δ 8.0 (d, *J* = 6.5 Hz, 1H), 7.33 (d, *J* = 8.7 Hz, 2H), 6.96 (d, *J* = 8.7 Hz, 2H), 5.98 (br s, 2H), 4.46 (s, 2H), 3.50–3.60 (m, 1H), 2.91 (br s, 1H), 1.97, 1.78 (dd, *J* = 10.9 Hz, *J* = 13.1 Hz, 4H), 1.36 (sext, 4H); ¹³C-NMR (DMSO-*d*₆): δ 167, 157, 129, 125, 117, 67, 49, 47, 31, 29; HPLC: *t*_R 2.03 min (95%).

6-Chloro-*N*-((1*r*,4*r*)-4-(2-(4-chlorophenoxy)acetamido)cyclohexyl)chromane-2-carboxamide (6; AAA1-084). To a stirred solution of (*rac*)-6-chlorochromane-2-carboxylic acid (**5**; 0.1 g, 0.5 mmol; prepared as described (32)) and Et₃N (0.13 mL, 1 mmol) in CH₂Cl₂ (5 mL) was added *O*-(benzotriazol-1-yl)-*N,N,N',N'*-tetramethyluronium hexafluorophosphate (HBTU; 0.21 g, 0.6 mmol). The mixture was stirred for 10 min, when **4b** (0.16 g, 0.55 mmol) was added. Stirring was continued overnight, the reaction was diluted with H₂O, and was extracted with EtOAc. The organic layer was washed with aq NH₄Cl and brine, dried over Na₂SO₄, filtered, and evaporated. The residue was triturated with Et₂O, collected, and dried to afford the title compound as an off-white powder (0.155 g, 65%). ¹H-NMR (DMSO-*d*₆): δ 7.95 (d, *J* = 8.2 Hz, 1H), 7.83 (d, *J* = 7.5 Hz, 1H), 7.35 (d, *J* = 8.3, 2H), 7.14 (d, *J* = 7.2, 2H), 6.97 (d, *J* = 9.3, 2H), 6.89 (d, *J* = 9.0 Hz, 1H), 4.51, 4.49 (dd, *J* = 3.9 Hz, *J* = 3.0 Hz, 1H), 4.46 (s, 2H), 3.59 (br s, 2H), 2.84–2.76 (m, 1H), 2.72–2.65 (m, 1H), 2.17–2.10 (m, 1H), 1.90–1.82 (m, 1H), 1.78 (br s, 4H), 1.40–1.30 (m, 4H); ¹³C-NMR (DMSO-*d*₆): δ 169, 168, 157, 152, 129, 126, 125, 124, 118, 117, 75, 67, 48, 31, 25, 23; HPLC: *t*_R 3.01 min (95%). HR-MS: *m/z* 477.1350 [M + H]⁺, C₂₄H₂₇Cl₂N₂O₄ requires 477.1342.

6-Chloro-*N*-((1*r*,4*r*)-4-(2-(4-chlorophenoxy)acetamido)cyclohexyl)-3,4-dihydro-2*H*-benzo[*b*][1,4]oxazine-2-carboxamide (8a; AAA1-075B). A solution of (*rac*)-ethyl 6-chloro-3,4-dihydro-2*H*-1,4-benzoxazine-2-carboxylate (**7a**; 0.25 g, 1 mmol; prepared as described (33)) in THF–H₂O (2:1) was treated with LiOH·H₂O (0.12 g, 3 mmol) and the resulting mixture was stirred for 3 h. The solution was neutralized with 1 M aq HCl solution and extracted with EtOAc. The organic phase was dried over Na₂SO₄, filtered and concentrated to afford 6-chloro-3,4-dihydro-2*H*-1,4-benzoxazine-2-carboxylic acid **7b** (0.19 g, 89%).

To a stirred solution of **7b** (0.15 g, 0.7 mmol) and Et₃N (0.18 mL, 1.4 mmol) in CH₂Cl₂ (5 mL) was added HBTU (0.3 g, 0.84 mmol). The mixture was stirred for 10 min, when **4b** (0.23 g, 0.77 mmol) was added. Stirring was continued overnight, the reaction was diluted with H₂O, and was extracted with EtOAc. The organic layer was washed with aq NH₄Cl and brine, dried over Na₂SO₄, filtered, and evaporated. The residue was dissolved in MeOH (1 mL) and the product was precipitated by addition of excess Et₂O. The precipitate was collected, washed with more Et₂O and dried to afford the title compound as an off-white powder (0.224 g, 67%). ¹H-NMR (DMSO-*d*₆): δ 8.08 (d, *J* = 8.4 Hz, 1H), 7.92 (d, *J* = 8.4 Hz, 1H), 7.34 (d, *J* = 8.7 Hz, 2H), 6.97 (d, *J* = 9.0 Hz, 2H), 6.78 (d, *J* = 8.4 Hz, 1H), 6.63 (d, *J* = 2.7 Hz, 1H), 6.50, 6.48 (dd, *J* = 3.3 Hz, *J* = 2.7 Hz, 1H), 6.31 (s, 1H), 4.47 (s, 2H), 4.44 (dd, *J* = 3.3 Hz, *J* = 3.6 Hz, 1H), 3.57 (br s, 2H), 3.45, 3.42 (tt, *J* = 6.7 Hz, *J* = 6.2 Hz, 1H), 3.20–3.15 (m, 1H), 1.78–1.70 (m, 4H), 1.42–1.29 (m, 4H); ¹³C-NMR (DMSO-*d*₆): δ 168, 166, 157, 141, 136, 129, 125, 118, 116, 114, 73, 68, 48, 42, 31; HPLC: *t*_R 2.90 min (95%). HR-MS: *m/z* 478.1286 [M + H]⁺, C₂₃H₂₆Cl₂N₃O₄ requires 478.1295.

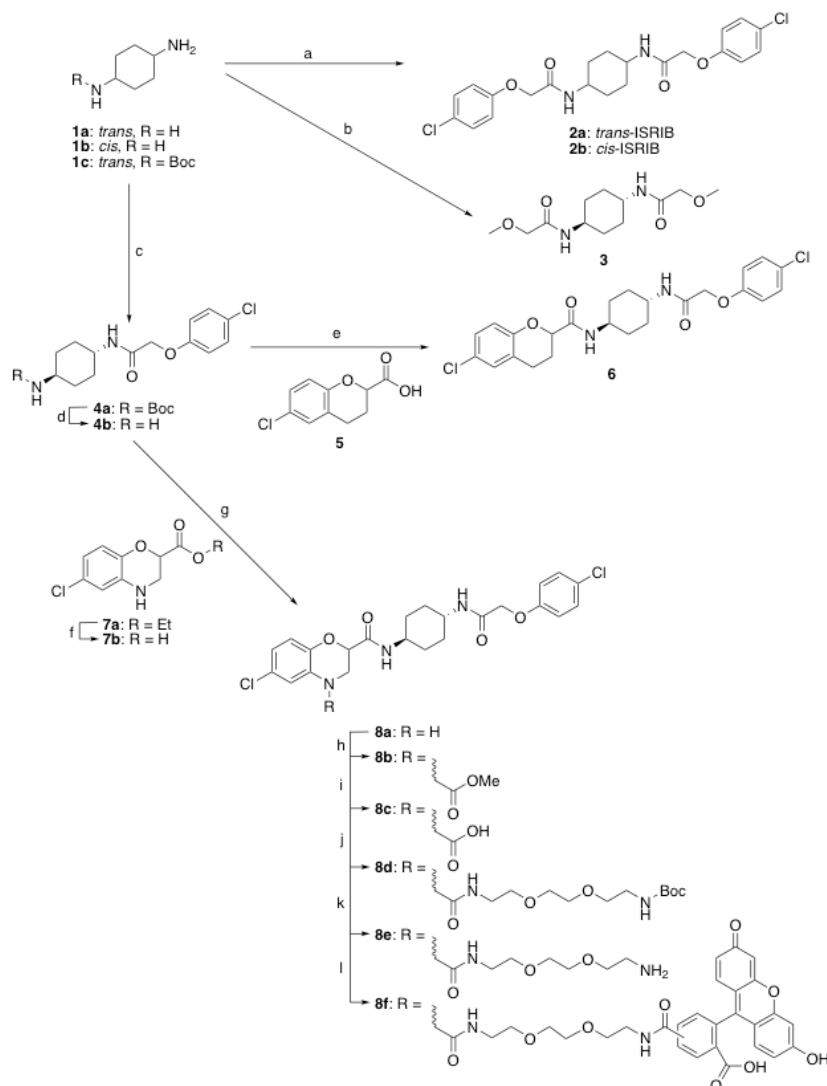
4- and 5-((2-(2-(2-(2-(6-Chloro-2-(((1*r*,4*r*)-4-(2-(4-chlorophenoxy)acetamido)cyclohexyl)carbamoyl)-2,3-dihydro-4*H*-benzo[*b*][1,4]oxazin-4-yl)acetamido)ethoxy)ethoxy)ethyl)carbamoyl)-2-(6-hydroxy-3-oxo-3*H*-xanthen-9-yl)benzoic acid (8f; AAA2-101). To a solution of **8a** (0.19 g, 0.4 mmol) in DMF (5 mL) was added K₂CO₃ (0.18 g, 1.2 mmol), NaI (0.09 g, 0.6 mmol), and methyl bromoacetate (0.1 mL, 0.48 mmol). The mixture was stirred at 125 °C for 16 h, cooled to room temperature, and diluted with H₂O (10 mL). The solution was extracted with EtOAc and the organic phase was washed with H₂O and brine, dried over Na₂SO₄, filtered, and evaporated. The residue was purified by silica gel column chromatography (CH₂Cl₂–THF gradient elution) to afford methyl ester **8b** (0.14 g, 65%).

A solution of **8b** (0.1 g, 0.18 mmol) in THF–H₂O (2:1) was treated with LiOH·H₂O (0.037 g, 0.9 mmol) and the resulting mixture was stirred for 3 h. The reaction was neutralized with 1 M aq HCl and extracted with EtOAc. The organic phase was dried over Na₂SO₄, filtered, and evaporated to afford the carboxylic acid derivative **8c** (0.09 g, 98%).

8c (0.09 g, 0.2 mmol) and Et₃N (0.06 mL, 0.5 mmol) were dissolved in CH₂Cl₂ (3 mL). HBTU (0.08 g, 0.22 mmol) was added and the mixture was stirred for 10 min, when *tert*-butyl (2-(2-(2-aminoethoxy)ethoxy)ethyl)carbamate (0.054 g, 0.22 mmol) in CH₂Cl₂ (1 mL) was added. The mixture was stirred overnight, diluted with H₂O, and extracted with EtOAc. The organic phase was washed with aq NH₄Cl and brine, dried over Na₂SO₄, filtered, and evaporated. The residue was purified by silica gel column chromatography (CH₂Cl₂–MeOH gradient elution) to afford the Boc-protected intermediate **8d** (0.12 g, 80%).

A solution of **8d** (0.12 g, 0.15 mmol) in dioxane (0.5 mL) was treated with 4 M HCl in dioxane (1 mL, 4 mmol). After stirring for 2 h the solution was evaporated. The residue was dissolved in MeOH (0.5 mL) and the product was precipitated by addition of excess Et₂O. The precipitate was collected and dried to afford the HCl salt of the amine derivative **8e** (0.10 g, 98%).

8c (14 mg, 0.02 mmol) and 5-(and 6-) carboxyfluorescein succinimidyl ester (9.4 mg, 0.02 mmol; NHS-fluorescein, 5/6-carboxyfluorescein succinimidyl ester mixed isomer (46410, ThermoFisher Scientific)), were dissolved in DMF (1 mL) with Et₃N (4 μL). The mixture was stirred overnight at 31 °C and was evaporated. The residue was fractionated by semi-preparative HPLC (Phenomenex Gemini 5 μm-110 Å, C₁₈, 150 x 10 mm column; 5 mL/min flow rate) with linear gradient elution of H₂O–MeCN (containing 0.1% HCOOH) from 85:15 to 5:95 over 13 min to afford the title compound **8f** as an orange powder (0.015 g, 75%). ¹H-NMR (DMSO-*d*₆): δ 8.88, 8.74 (tt, *J* = 5.8 Hz, *J* = 11.7 Hz, 1H), 8.46 (s, 1H), 8.30 (br s, 1H), 8.22, 8.15 (dd, *J* = 8.6 Hz, *J* = 8.0 Hz, 1H), 8.05-8.11 (m, 1H), 7.96 (t, *J* = 8.1 Hz, 2H), 7.68 (s, 1H), 7.34 (t, *J* = 9.7 Hz, 2H), 6.95 (d, *J* = 8.6 Hz, 2H), 6.82 (d, *J* = 8.6 Hz, 1H), 6.67 (s, 2H), 6.58 (d, *J* = 8.9 Hz, 2H), 6.54 (s, 2H), 6.49 (d, *J* = 8.0 Hz, 1H), 4.61 (quint, *J* = 4.0 Hz, 1H), 4.44 (s, 2H), 4.44, 3.81-3.96 (m, 4H), 3.5-3.57 (m, 8H), 2.07 (s, 2H), 1.67-1.78 (m, 4H), 1.29-1.39 (m, 4H), 1.23 (s, 4H); HPLC: *t*_R 2.81 min (95%); HR-MS: *m/z* 1024.2920 [M + H]⁺, C₅₂H₅₂C₁₂N₅O₁₃ requires 1024.2933.



Scheme S4. (a) **1a** or **1b**, 4-chlorophenoxyacetyl chloride, iPr_2NEt , CH_2Cl_2 , 0 °C to rt (70-88%); (b) **1a**, methoxyacetyl chloride, iPr_2NEt , CH_2Cl_2 , 0 °C to rt (85%); (c) **1c**, 4-chlorophenoxyacetyl chloride, iPr_2NEt , CH_2Cl_2 , 0 °C to rt (95%); (d, f, and k) 4 M HCl in dioxane–MeOH (89-98%); (e) **4b** and **5**, HBTU, Et_3N , CH_2Cl_2 (65%); (g) **4b** and **7b**, HBTU, Et_3N , CH_2Cl_2 (67%); (h) methyl bromoacetate, K_2CO_3 , NaI, DMF, 125 °C, 16 h (65%); (i) LiOH, THF– H_2O (98%); (j) *tert*-butyl (2-(2-(2-aminoethoxy)ethoxy)ethyl)carbamate, HBTU, Et_3N , CH_2Cl_2 (80%); (l) 5-(and 6-) carboxyfluorescein, iPr_2NEt , DMF, 31 °C, 12 h (75%).

Fig. S1

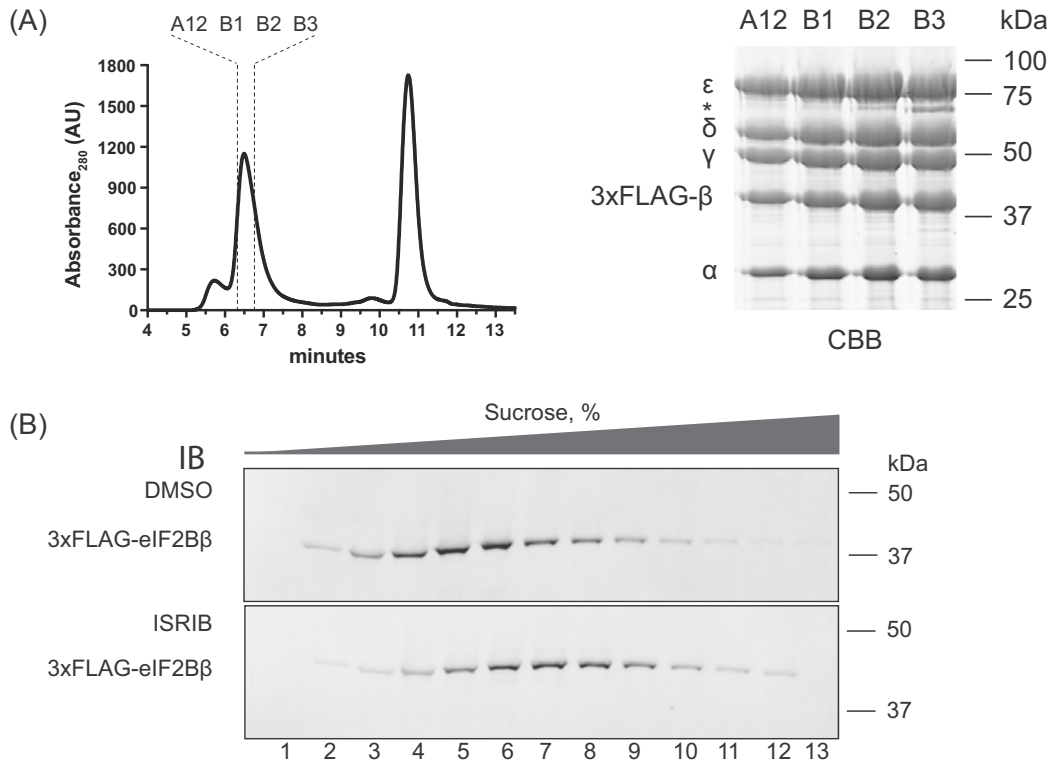


Figure S1
Biochemical analysis of human eIF2B

(A) Chromatogram of endogenous human eIF2B purified from HeLa cells with 3xFLAG-tag (introduced by homologous recombination into the *EIF2B2* locus), resolved by size exclusion chromatography on a SEC-3 300 Å chromatography column (left panel). The indicated fractions were analyzed on a Coomassie-stained SDS-PAGE gel (right panel, the asterisks * indicates PRMT5 – a contaminant) and used in structural analysis.

(B) Immunoblot of 3xFLAG-tagged eIF2Bβ detected with anti-FLAG M2 antibodies in HeLa cell lysates that were either treated with DMSO (top panel) or ISRIB (200 nM) (bottom panel) and resolved on a 5-20% sucrose density gradient. The observed shift of 3xFLAG-eIF2Bβ signal towards HMW fractions reflects the stabilizing effect of ISRIB on the protein complex (compare top and bottom panels) (performed once, confirming the findings of (9)).

Fig. S2

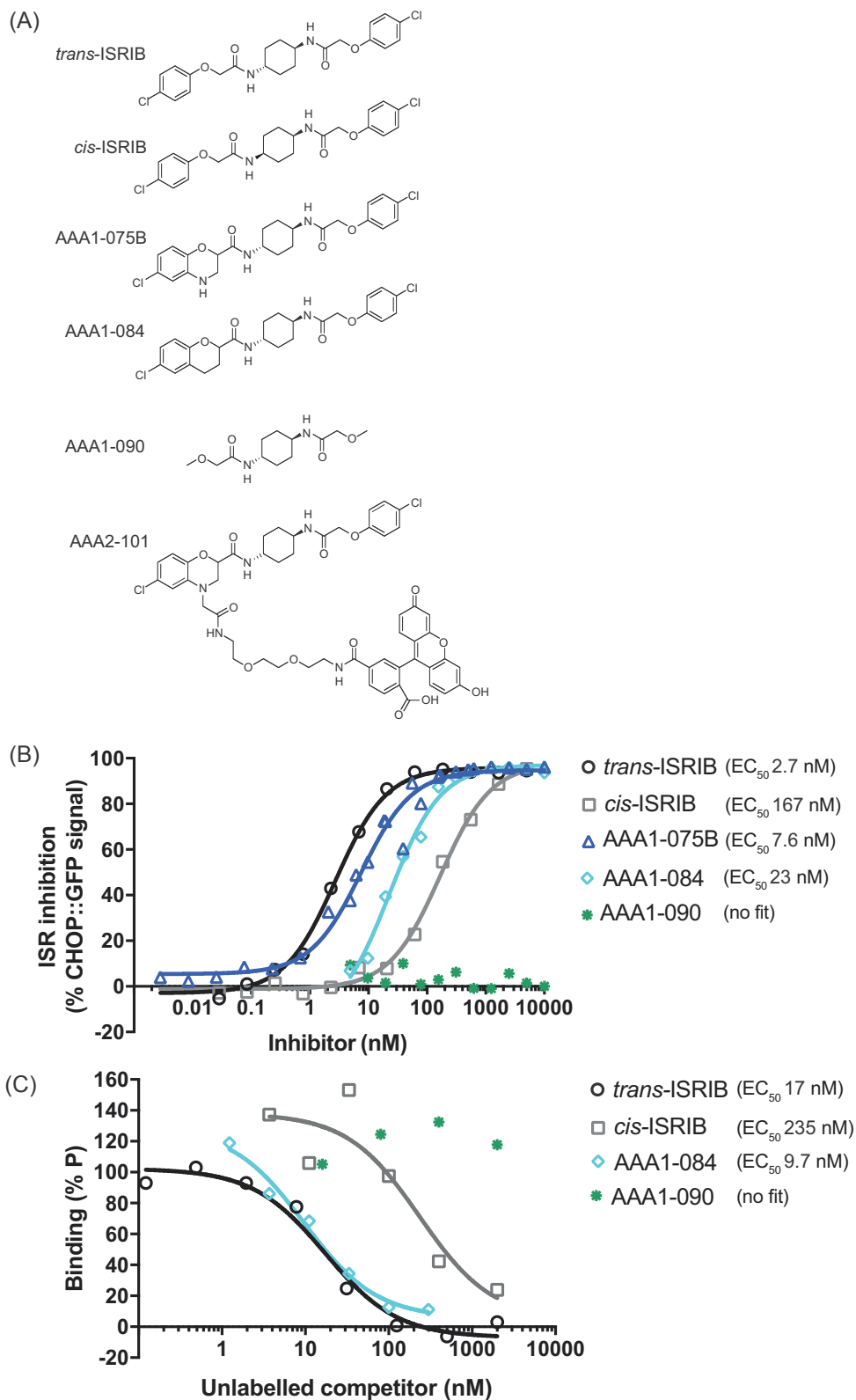


Figure S2

ISRIB and its analogs inhibit the ISR in cells and bind eIF2B in vitro

(A) Structures of ISRIB and ISRIB analogs used in this study: active trans-ISRIB, cis-ISRIB, the reference analogs AAA1-075B and AAA1-084, the inactive AAA1-090 and fluorescein-labeled AAA2-101 used in the fluorescence polarization experiments.

(B) Plot of the inhibition of the Integrated Stress Response (ISR) activated CHOP::GFP signal, induced upon treatment of CHO-K1 cells with histidinol (HIS) (0.5 mM), in the presence of escalating concentrations of trans and cis-ISRIB. Shown is a representative from three independent experiments conducted for trans and cis-ISRIB and of single experiment conducted for analogs. Concentration of inhibitor is represented on a log₁₀ scale. Curve fitting and EC₅₀ was generated using agonist vs. response function on GraphPad Prism.

(C) Plot of the FP signal arising from samples with fluorescein-labeled AAA2-101 (100 nM) bound to purified human eIF2B (250 nM) in the presence of the indicated concentration of unlabeled ISRIB analogs introduced as competitors. Shown is a representative from three independent experiments. Concentration of inhibitor is represented on a log₁₀ scale. Curve fitting and EC₅₀ was generated using agonist vs. response function on GraphPad Prism.

Fig. S3

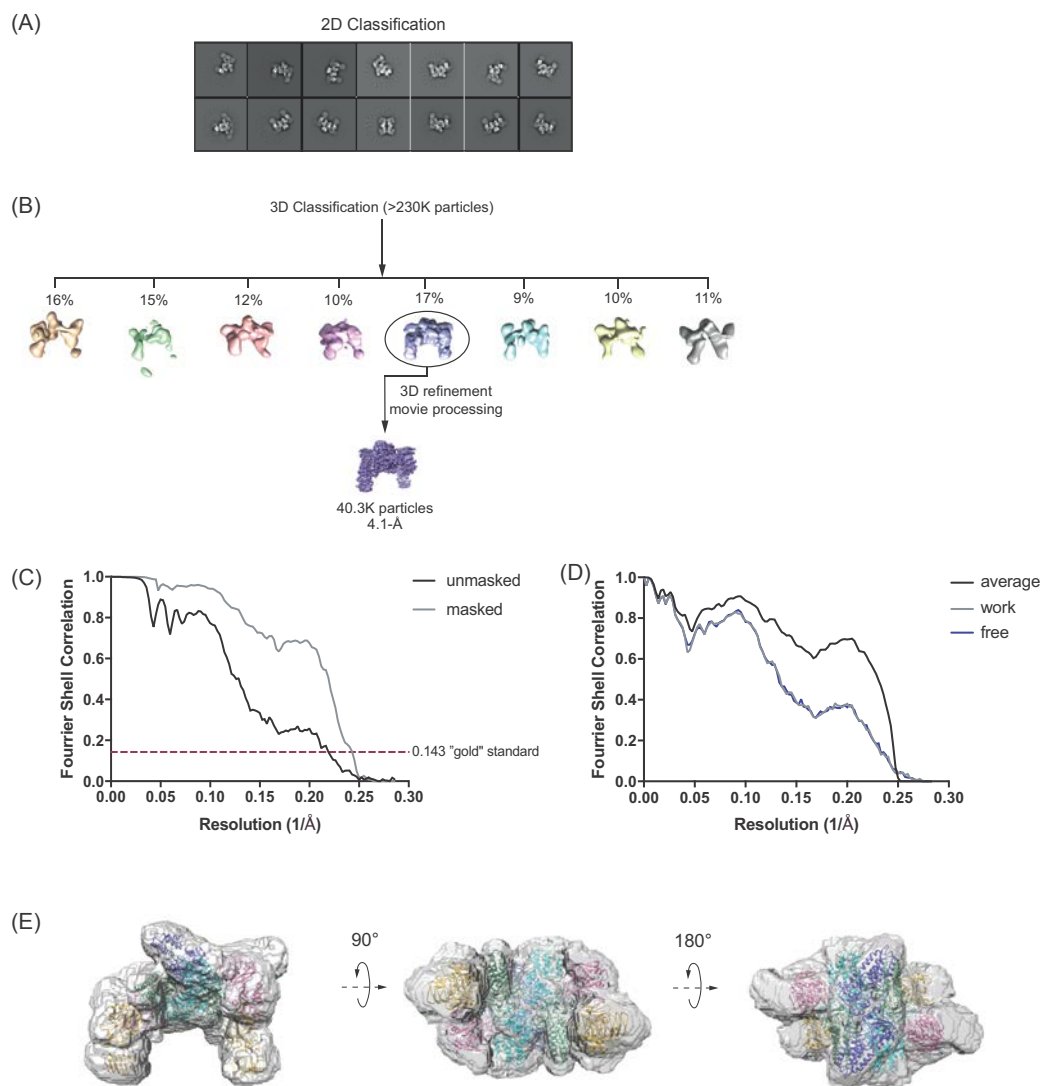


Figure S3

Cryo-electron microscopy data processing

(A) Representative sample of the reference-free 2D class averages of eIF2B particles used for 3D classification and initial model generation. Analysis was performed using RELION and EMAN2 software.

(B) After 3D classification was conducted on the whole particle dataset (237,213), 17% (40,326 particles) were used to generate and refine the final 3D map. Analysis was performed using RELION.

(C) Gold-standard Fourier shell correlation (FSC) curves. Unmasked map FSC curve is represented in black. Masked-corrected map FSC curve is represented in grey and crosses the 0.143 'gold standard' purple line at a resolution of 4.1 Å indicating the resolution of the masked map.

(D) Refinement and cross-validation of the eIF2B model. The final map vs. model 'FSC average' curve is represented in black. For cross-validation, the model was 'shaken' (see Methods section) and refined against one of the two half-maps to generate the 'FSC work' curve (grey line). The 'FSC free' curve was calculated between this same refined model and the other half-map (blue line). Superimposition of the two FSC curves shows no sign of over-fitting.

(E) Transparent representations of the "soft" mask used for post-processing of the final density map. eIF2B subunits are represented in cartoon and colored as in Fig. 1B, C.

Fig. S4

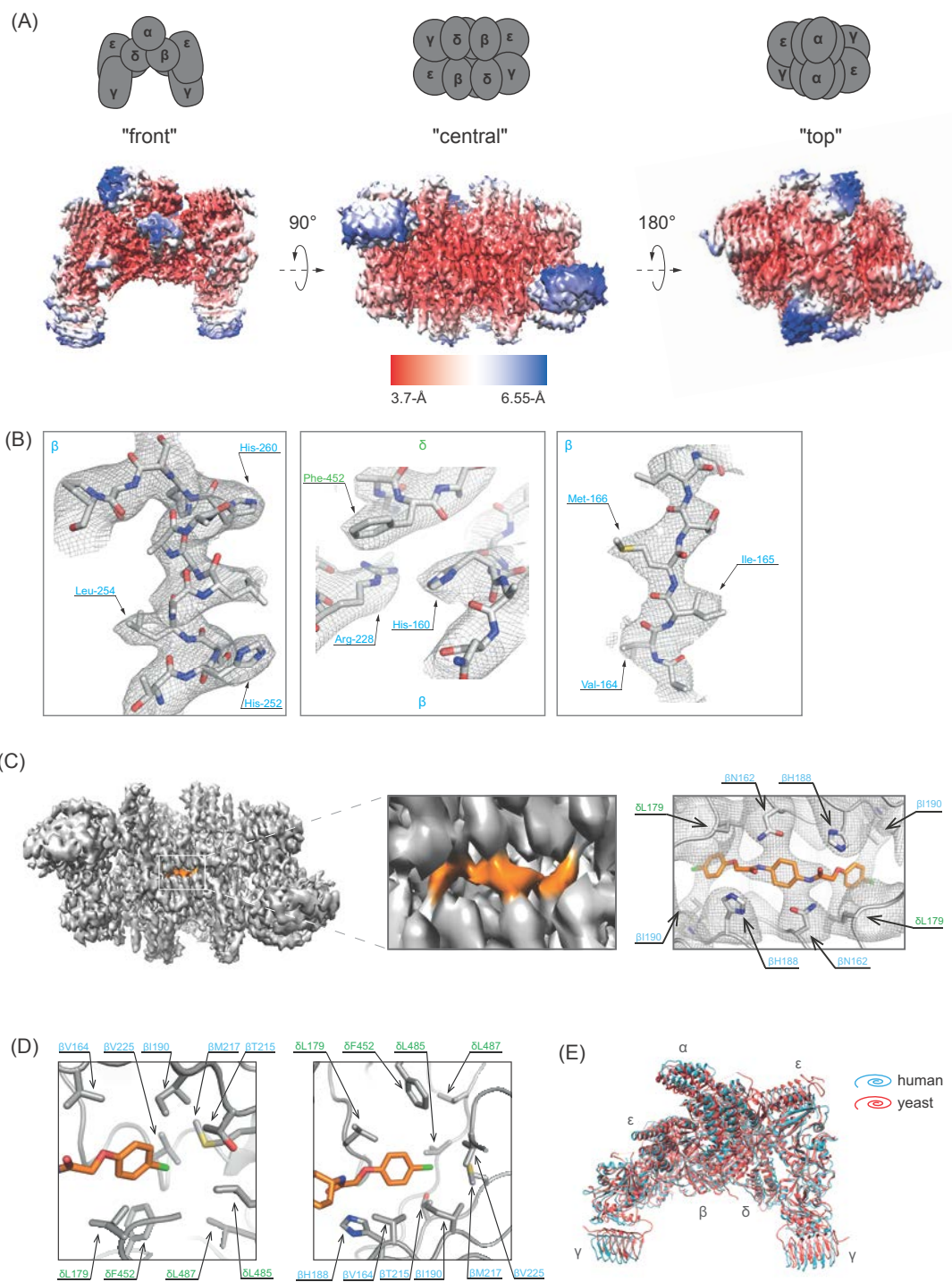


Figure S4

Structure of the ISRIB-bound human eIF2B

(A) Density map colored according to local resolution for the ISRIB-bound eIF2B complex. The highest resolution is at the core of the $(\beta\delta)_2$ dimer interface, where the putative density of ISRIB was detected. The red-blue palette covers resolution range from 3.7 Å to >6.55 Å.

(B) Representative density depicted as a mesh around the eIF2B atomic model including well-resolved side chains from the core of $(\beta\delta)_2$ dimer interface. Individual residues of β (blue) and δ (green) subunits are labeled for reference.

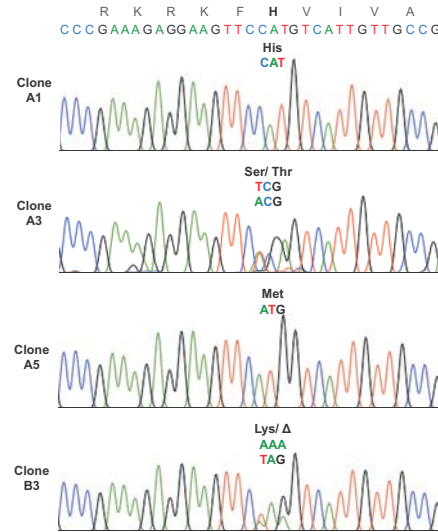
(C) Left: cryo-EM map of human eIF2B bound to ISRIB (“central” view). The ISRIB density is shown in orange. Right: close up of the “central” view showing density corresponding to ISRIB at the $(\beta\delta)_2$ dimer interface, without and with the superimposed model. Residues contacting ISRIB in the central part of the pocket from the β (blue) and δ (green) subunits are indicated. ISRIB is represented as orange sticks.

(D) Close-up of the hydrophobic end of the pocket. Two views of the eIF2B complex core are presented, showing the symmetrically opposite sides of the pocket. The left panel view is from the solvent area looking at the core of the protein. The right panel is from the core looking at the solvent area.

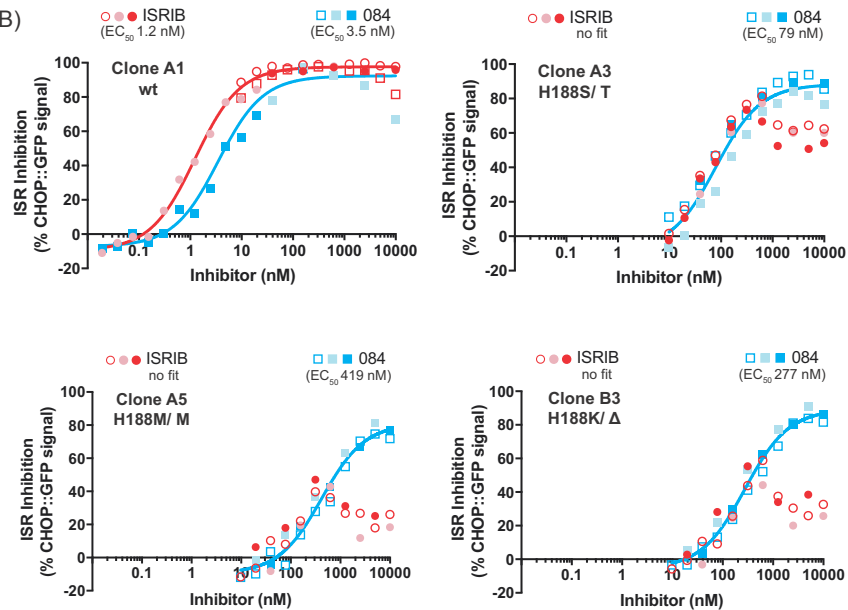
(E) Superimposition of ISRIB-bound human (cyan) and yeast eIF2B (lacking bound ISRIB, PDB: 5B04, (10), red) from the “front view”.

Fig. S5

(A)



(B)

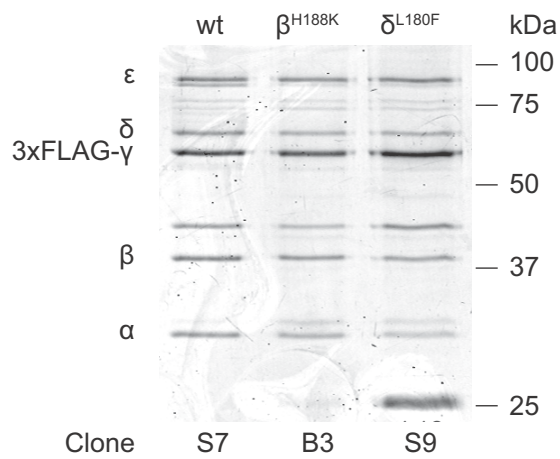
**Figure S5**

Individual clones from 084^{SEN} pool recapitulate the variation in sensitivity to ISRIB and AAA1-084 observed in ISRIB^{RES} pool of *Eif2b2*^{H188X}

(A) Traces of dye-termination sequencing reactions of PCR amplified *Eif2b2* exon 3 from indicated cell clones: A1 (parental, wt), A3 (H188S/T), A5 (H188M), B3 (H188K/Δ). H188 is highlighted.

(B) Graphs showing inhibition of the ISR-activated CHOP::GFP signal, induced upon treatment with HIS (0.5 mM), by ISRIB and AAA1-084 (084) in individual clones from 084^{SEN} pool (from Figure 3B). Shown is data from three independent experiments for each of the compounds. Concentration of ISRIB is represented on a log₁₀ scale. Curves fitting and EC₅₀ was generated using agonist vs. response function on GraphPad Prism.

Fig. S6

**Figure S6****Biochemical characterization of purified hamster eIF2B**

Coomassie stained SDS-PAGE gel of endogenous hamster eIF2B purified from wildtype (wt, clone A1), *Eif2b2*^{H188K} (clone B3) and *Eif2b4*^{L180F} (clone S9) CHO cells via a 3xFLAG-tag knocked into *Eif2b3* locus (encoding the γ subunit).

Table S1. Cell lines

Gene	Exon	Cells	Clone name	Description	Mutagenized region (number shows amino acid position at which mutagenesis occurred)
<i>Eif2b3</i>	11	CHO-K1	S9	eif2b3-3xFLAG-tagged ISRIB-resistant (L180F) cells	451_EFCRYPAQWRPLERADYKDHDGDKDHDIDYKDDDDK*
<i>Eif2b2</i>	3	CHO-K1	N162X	mixed population of ISRIB-resistant cells	162_XEVIMTIGYSRTVEAFLEAARKRKFHVIV
<i>Eif2b2</i>	3	CHO-K1	H188X	mixed population of ISRIB-resistant cells	188_XVIVAEAPFCQVRG
<i>Eif2b2</i>	3	CHO-K1	I190X	mixed population of ISRIB-resistant cells	190_XVIVAEAPFCQVRG
<i>Eif2b2</i>	3	CHO-K1	H188X-075B	mixed population of 075B-sensitive cells	188_XVIVAEAPFCQVRG
<i>Eif2b2</i>	3	CHO-K1	H188X-084	mixed population of 084-sensitive cells	188_XVIVAEAPFCQVRG
<i>Eif2b2</i>	3	CHO-K1	A3	H188S/T, heterozygous, 084-sensitive, mildly ISRIB-resistant	188_SVIVAEAPFCQVRG; 188_TVIVAEAPFCQVRG
<i>Eif2b2</i>	3	CHO-K1	A5	H188M, homozygous, 084-sensitive, strongly ISRIB-resistant	188_MVIVAEAPFCQVRG
<i>Eif2b2</i>	3	CHO-K1	B3	H188K/Δ, heterozygous, 084-sensitive, strongly ISRIB-resistant	188_KVIVAEAPFCQVRG

Table S2. Oligonucleotide list

ID	Primer name	Sequence	Description	Figure
Oligo1922	EIF2B2_H188X_ssODN_S	CTCTGGAGCACATCACTCCAATGAGGTGATGACCATTTGGCTATTCTAGAACAGTAGAAGCCTTCTTAAAGAGGCAGCCCGAAAGAGGAAGTTCNNNGTCATTGTTGCCGAGTGTGCTCCCTTCTGCCAGGTAAGAGGGGGCTGCTAAGAGTTGCTAAGAAAAGGTGAAGAGGGAATAAATAAAGGAGGAATGGAG	sense single strand ODN repair template for <i>Eif2b</i> H188X clone	2
Oligo1923	EIF2B2_I190X_ssODN_S	CTGGAGCACATCACTCCAATGAGGTGATGACCATTTGGCTATTCTAGAACAGTAGAAGCCTTCTTAAAGAGGCAGCCGAAAGAGGAAGTTCATGTCCNNNGTTCGCCGAGTGTGCTCTTCTGCCAGGTAAGAGGGGGCTGCTAAGAGTTGCTAAGAAAAGGTGAAGAGGGAATAAATAAAGGAGGAATGGAGTGA	sense single strand ODN repair template for <i>Eif2b</i> I190X clone	2
Oligo1924	EIF2B2_N162X_ssODN_AS	GAGCACACTCGGCAACAATGACATGGAACTCTCTTTCGGGCTGCTCTTAAAGGAAGGCTTCTACTGTTCTAGAATAGCCATGTCATGATCCTNNNGGAGTGGATGTGCTCCAGAGCTTGGGCTGCAATGTTCTCCGTTGCTCTGCAAGAACAGTTTGAAGGGAATGTGAAACGGCCATGCTTCATC	anti-sense single strand ODN repair template for <i>Eif2b</i> N162X clone	2
Oligo1925	EIF2B2_Exon3_Guide7_S	CACCGGGAGCACATCACTCCAATG	sense oligo for Guide7 targeting hamster <i>Eif2b</i> exon 3 (for UK2105 plasmid)	2
Oligo1926	EIF2B2_Exon3_Guide7_AS	AAACCATTGGAGTGGATGTGCTCCC	anti-sense oligo for Guide7 targeting hamster <i>Eif2b</i> exon 3 (for UK2105 plasmid)	2
Oligo1927	EIF2B2_Exon3_Guide8_S	CACCGCACACTCGGCAACAATGACA	sense oligo for Guide8 targeting hamster <i>Eif2b</i> exon 3 (for UK2106 plasmid)	2
Oligo1928	EIF2B2_Exon3_Guide8_AS	AAACTGTCTGTTGCCGAGTGTGC	anti-sense oligo for Guide8 targeting hamster <i>Eif2b</i> exon 3 (for UK2106 plasmid)	2
Oligo1759	pKLV_NEBNXT01_1759	CAAGCAGAAGACGGCATAACGAGATCGTGACTGGAGTTACAGACGTGTGCTCTCCGATCTGAGGCCACTTGTGTAGCGCCAAG	barcoding primer for NGS	2B, 3B
Oligo1760	pKLV_NEBNXT02_1760	CAAGCAGAAGACGGCATAACGAGATCGTGACTGGAGTTACAGACGTGTGCTCTCCGATCTGAGGCCACTTGTGTAGCGCCAAG	barcoding primer for NGS	2B, 3B
Oligo1761	pKLV_NEBNXT04_1762	CAAGCAGAAGACGGCATAACGAGATCGTGACTGGAGTTACAGACGTGTGCTCTCCGATCTGAGGCCACTTGTGTAGCGCCAAG	barcoding primer for NGS	2B, 3B
Oligo1762	pKLV_NEBNXT05_1763	CAAGCAGAAGACGGCATAACGAGATCGTGACTGGAGTTACAGACGTGTGCTCTCCGATCTGAGGCCACTTGTGTAGCGCAAG	barcoding primer for NGS	2B, 3B
Oligo1763	pKLV_NEBNXT06_1764	CAAGCAGAAGACGGCATAACGAGATCGTGACTGGAGTTACAGACGTGTGCTCTCCGATCTGAGGCCACTTGTGTAGCGCCAAG	barcoding primer for NGS	2B, 3B
Oligo1764	pKLV_NEBNXT07_1765	CAAGCAGAAGACGGCATAACGAGATCGTGACTGGAGTTACAGACGTGTGCTCTCCGATCTGAGGCCACTTGTGTAGCGCCAAG	barcoding primer for NGS	2B, 3B
Oligo1765	pKLV_NEBNXT08_1766	CAAGCAGAAGACGGCATAACGAGATCGTGACTGGAGTTACAGACGTGTGCTCTCCGATCTGAGGCCACTTGTGTAGCGCCAAG	barcoding primer for NGS	2B, 3B
Oligo1766	pKLV_NEBNXT09_1767	CAAGCAGAAGACGGCATAACGAGATCGTGACTGGAGTTACAGACGTGTGCTCTCCGATCTGAGGCCACTTGTGTAGCGCCAAG	barcoding primer for NGS	2B, 3B
Oligo1767	pKLV_NEBNXT10_1768	CAAGCAGAAGACGGCATAACGAGATCGTGACTGGAGTTACAGACGTGTGCTCTCCGATCTGAGGCCACTTGTGTAGCGCCAAG	barcoding primer for NGS	2B, 3B
Oligo1775	P1_pKLV-EIF2B2_1975	TGAGGCCACTTGTGAGGCCAAGTGCAGAAGGCACAACGGAGAAC	adaptor primer for NGS	2B, 3B
Oligo1776	P2 EIF2B2_NGS_1976	ACACTCTTCCCTACACGACGCTCTCCGATCTTACAGACCCCTCTTACCTGGC	adaptor primer for NGS	2B, 3B
Oligo1777	P5_Truseq Universal_1977	AATGATACGGGACACCGAGATCTACACTCTTCCCTACACGACGCTCTCCGATCT	adaptor primer for NGS	2B, 3B

Table S3. Plasmid list

ID	Plasmid name	Description	Primers used to generate plasmid	Figure
UK2105	EIF2B2_CRISPR7_pSpCas9(BB)-2A-mCherry	mCherry-tagged CRISPR/Cas9 plasmid with guide RNA for targeting hamster <i>Eif2b2</i> exon 3 bottom strand	Oligo1925 Oligo1926	2
UK2106	EIF2B2_CRISPR8_pSpCas9(BB)-2A-mCherry	mCherry-tagged CRISPR/Cas9 plasmid with guide RNA for targeting hamster <i>Eif2b2</i> exon 3 top strand	Oligo1927 Oligo1928	2

Table S4. Allele frequency (Fig. 2B)

Amino Acid	N162X				H188X				I190X			
	ISRIB-SEN		ISRIB-RES		ISRIB-SEN		ISRIB-RES		ISRIB-SEN		ISRIB-RES	
	Reads	% Reads										
*	855	0.20	6575	1.74	1025	0.31	6215	2.48	340	0.09	3467	1.23
A	3953	0.92	1768	0.47	2248	0.69	4305	1.72	1106	0.31	1213	0.43
C	2429	0.57	1654	0.44	5992	1.83	716	0.29	1416	0.39	3145	1.12
D	3953	0.92	1436	0.38	662	0.20	5075	2.03	419	0.12	5912	2.10
E	2655	0.62	867	0.23	227	0.07	8902	3.55	426	0.12	574	0.20
F	2064	0.48	2798	0.74	8730	2.66	682	0.27	3363	0.93	10199	3.62
G	419	0.10	26632	7.05	965	0.29	52762	21.05	949	0.26	5716	2.03
H	9410	2.20	10487	2.78	269253	82.06	6443	2.57	208	0.06	1315	0.47
I	2804	0.66	14912	3.95	4980	1.52	1749	0.70	326077	90.10	39307	13.96
K	3520	0.82	2809	0.74	499	0.15	20494	8.18	139	0.04	359	0.13
L	10772	2.52	7055	1.87	1794	0.55	46099	18.39	8405	2.32	5827	2.07
M	1211	0.28	724	0.19	350	0.11	4795	1.91	192	0.05	68523	24.34
N	350813	82.08	165829	43.92	3058	0.93	668	0.27	398	0.11	770	0.27
P	2485	0.58	11242	2.98	425	0.13	648	0.26	331	0.09	947	0.34
Q	5727	1.34	1589	0.42	443	0.14	15550	6.21	207	0.06	2403	0.85
R	7597	1.78	8707	2.31	411	0.13	59827	23.87	548	0.15	2188	0.78
S	8007	1.87	9712	2.57	2208	0.67	8331	3.32	829	0.23	4443	1.58
T	2143	0.50	99150	26.26	1737	0.53	3153	1.26	452	0.12	1932	0.69
V	1721	0.40	2101	0.56	13035	3.97	2950	1.18	15627	4.32	1749	0.62
W	428	0.10	142	0.04	4038	1.23	618	0.25	147	0.04	79154	28.11
X	253	0.06	209	0.06	329	0.10	256	0.10	63	0.02	48	0.02
Y	4159	0.97	1146	0.30	5704	1.74	379	0.15	262	0.07	42391	15.05
Total Reads	427378		377544		328113		250617		361904		281582	

Table S5. Allele frequency (Fig. 3B)

Amino Acid	H188X ISRIB-RES							
	ISRIB-RES		ISRIB-SEN		075B-SEN		084-SEN	
	Reads	% Reads	Reads	% Reads	Reads	% Reads	Reads	% Reads
*	8309	2.64	648	0.22	4001	1.88	4428	1.63
A	5809	1.85	4595	1.56	16814	7.89	23876	8.78
C	1346	0.43	3465	1.17	1687	0.79	2635	0.97
D	4608	1.47	797	0.27	2338	1.10	3892	1.43
E	8292	2.64	920	0.31	1228	0.58	1311	0.48
F	1776	0.57	12004	4.06	2450	1.15	3853	1.42
G	52131	16.59	1558	0.53	10887	5.11	12264	4.51
H	9311	2.96	226030	76.53	34473	16.18	55443	20.40
I	2684	0.85	4081	1.38	3612	1.70	4906	1.81
K	27535	8.76	803	0.27	47373	22.24	44470	16.36
L	67765	21.56	6498	2.20	13552	6.36	12728	4.68
M	6690	2.13	666	0.23	11051	5.19	8943	3.29
N	772	0.25	1915	0.65	1587	0.75	1816	0.67
P	1193	0.38	1520	0.52	1038	0.49	1298	0.48
Q	22530	7.17	1111	0.38	4152	1.95	6029	2.22
R	71454	22.74	1397	0.47	6097	2.86	7651	2.82
S	11841	3.77	4824	1.63	31921	14.98	49558	18.23
T	4857	1.55	3513	1.19	11650	5.47	15931	5.86
V	3537	1.13	11438	3.87	5317	2.50	7625	2.81
W	1177	0.37	4767	1.61	1123	0.53	2019	0.74
X	61	0.02	61	0.02	48	0.02	56	0.02
Y	613	0.20	2757	0.93	654	0.31	1105	0.41
Total Reads	314291		295368		213053		271837	

Table S6. Data collection, map reconstruction, and model statistics

Cryo-electron microscopy data collection	
Electron microscope	Titan Krios 300 kV
Detector	FEI Falcon II
Detector mode	Linear
Pixel size (Å)	1.75
Defocus range (µm)	-2.5 to -3.5
Dose rate (e ⁻ .pixel ⁻¹ .s ⁻¹)	60
Electron dose (e ⁻ .Å ⁻² .s ⁻¹)	20
Exposure time (s)	1.5
Total dose (e ⁻ .Å ⁻²)	30
Movies	765
Frames / movie	25
Reconstruction	
Software	Relion
Symmetry	C2
Particles used for 3D refinement	41750
Cell dimensions	
a, b, c (Å)	240, 240, 240
A, β, γ (°)	90, 90, 90
Model refinement	
Resolution limit	4.1
Map sharpening factor (Å ²)	-140.4
FSC _{average} ¹	0.6931
RMS bonds deviation (Å)	0.0069
RMS angles deviation (Å)	1.3485
Model validation	
Molprobity score	2.33 (99th percentile)
Clashscore	6.84 (100th percentile)
Ramachandran favored	80.68%
Ramachandran allowed	18.57%
Ramachandran outliers	0.75%
Rotamer favored	91.44%
Rotamer outliers	0.20%

¹ $FSC_{average} = \Sigma(N_{shell} FSC_{shell} / \Sigma(N_{shell}))$, where FSC_{shell} is the FSC in a given shell, N_{shell} is the number of 'structure factors' in the shell. $FSC_{shell} = \Sigma(F_{model} FEM) / (\sqrt{\Sigma(|F|^2_{model})} \sqrt{\Sigma(F^2_{EM}))}$.